J. Fluid Mech. (2005), *vol.* 529, *pp.* 311–347. © 2005 Cambridge University Press
doi:10.1017/S0022112005003472 Printed in the United Kingdom

Free-surface fluctuations behind microbreakers: space–time behaviour and subsurface flow field

By A. IAFRATI AND E. F. CAMPANA

INSEAN – The Italian Ship Model Basin, Roma, Italy

(Received 18 June 2003 and in revised form 6 December 2004)

The unsteady development toward breaking of the wavy flow generated by a submerged hydrofoil starting from rest is investigated numerically by solving the two-dimensional Navier–Stokes equations for the two-phase flow of air and water and by using a level-set technique to capture the interface. The study, carried out for hydrofoils with various chord lengths, shows that, when passing from longer to shorter scales, the role played by surface tension becomes more and more relevant and different flow regimes are recovered ranging from intense plunging jet, eventually leading to a large amount of entrapped air, down to microscale breakers, in which the jet is replaced by a bulge growing on the wave crest and the breaking event takes place without air entrapment. The ‘toe’ of the bulge slides down upon the forward face of the wave and large downstream-propagating surface fluctuations are observed. Wavenumber and frequency spectra of the computed free-surface profiles, aimed at understanding the downstream motion of free-surface fluctuations, are evaluated and found in good agreement with similar investigations carried out experimentally and available in literature.

A careful inspection of the instantaneous vorticity field under the microbreakers reveals the presence of an intense shear flow originating at the toe, instability of which eventually gives rise to coherent vortex-structures. These structures are convected downstream by the flow at a growing speed, remaining confined in a thin layer just beneath the free surface. This continuous interaction is responsible for the generation of the free-surface fluctuations experimentally found.

1. Introduction

In the present paper the free surface and the flow-field evolution from the initial establishment of breaking waves up to the post-breaking quasi-steady state are numerically investigated with attention mainly focused on small-scale waves. Brocchini & Peregrine (2001) proposed a tentative description aimed at classifying the different flow regimes that take place in spilling breakers observable in nature, ranging from strongly distorted free surface, with creation of drops and bubbles, down to low turbulence levels for which the stabilizing effect of gravity and surface tension prevents air being entrapped into the liquid. The latter regime, which is referred to as knobbly flow, is of primary interest in the following.

Changes in the flow features induced by the increasing surface tension contribution when reducing the length scale have been numerically analysed by Tulin (1996). The study, carried out within the potential flow assumption, simulated the development of breaking events in two-dimensional wavetrains caused by unstable side-bands introduced at the wakemaker about the central frequency. In that study, it is shown that surface tension effects become visible for wavelength corresponding to the central frequency shorter than 2 m and, for wavelengths shorter than 50 cm, the overturning process characterizing plunging breakers is entirely suppressed. The breaking region takes a bore-like structure with a well-defined initial point, usually called 'toe', and a train of capillary waves appears in front of it. Owing to the different mechanism for wave-breaking development, the amount of entrained air is significantly reduced (Duncan 2001).

In open sea, short-wavelength spilling breakers, also referred to as 'microbreakers' by Banner & Phillips (1974), are usually caused by the wind and play an important role in terms of momentum, heat and gas exchange between atmosphere and oceans (Jessup, Zappa & Yeh 1997; Melville 1996). Short-scale wind-waves have been experimentally investigated in the laboratory by Okuda (1982) and Ebuchi, Kawamura & Toba (1987), among others. Through accurate flow visualizations, the occurrence of an intense vorticity field at the wave crest has been revealed by Okuda (1982) to be a defining feature of microbreakers. In Ebuchi *et al.* (1987), the free-surface configurations taking place in the presence of wind have been measured by using an optical method and the bore-structure of the breaking crest is highlighted along with the formation of a capillary wavetrain ahead of the toe and the occurrence of streamwise streaks on the backward face of the crest. A possible explanation has been proposed by Longuet-Higgins (1992) who speculated that, for steep capillary waves, the flow separates at the wave trough ahead of the bulge, giving rise to an intense vorticity field inside the bulge. For milder waves, flow separation does not occur and no strong vortical roller is formed at the crest. Vorticity is only generated by the free-surface curvature, and is thus much weaker and of opposite sign (Mui & Dommermuth 1995). A numerical study of the capillary ripples developing in front of short waves has been carried out by Ceniceros (2003) where the vorticity field beneath the free surface is carefully analysed and the role played by surfactants on the vorticity field and on the ripple formation is investigated.

To gain more insight into the flow field taking place inside the bulge, small-scale spilling breakers have been produced by using the dispersive focusing technique (Rapp & Melville 1990; Duncan *et al.* 1994) and by towing a hydrofoil beneath the free surface (Lin & Rockwell 1995; Duncan & Dimas 1996). In Duncan *et al.* (1994), very gentle breakers have been achieved by progressively reducing the amplitude of the wavemaker motion. It is shown that, at an early stage, the bulge grows while the toe is substantially fixed with respect to the bulge. In a next stage, the toe begins to slide down upon the forward face of the wave and a train of downstream-propagating free-surface fluctuations appears between the toe and the crest. A plausible explanation for this phenomenon has been proposed by Longuet-Higgins (1994) who introduced a distinction between the capillary ripples in front of the bulge (Type I) and the downstream propagating free-surface fluctuations, classified as Type II. According to Longuet-Higgins, these latter are produced by the instabilities of the vorticity shed by the highly curved troughs of the capillary wave system ahead of the toe.

A better understanding of the mechanisms responsible for the formation of downstream propagating fluctuations has been provided by Duncan *et al.* (1999) and Qiao & Duncan (2001). In those studies, an accurate experimental investigation of the evolution of the free-surface profiles and of the flow field beneath is presented, showing that no vorticity appears within the bulge until the toe motion begins. As soon as the toe experiences its motion, a shear layer develops between the gravity-induced downslope flow near the free surface and the underlying upslope flow. Instabilities of this shear layer eventually develop into a train of downstream-propagating free-surface fluctuations coming out between the toe and the crest of the bulge.

The velocity field observed in this unsteady breaking process has some resemblance to that experimentally observed by Lin & Rockwell (1995) beneath the steady breakers produced by a hydrofoil. Flow measurements by a particle image velocimetry (PIV) technique give evidence of the shear flow that arises from the toe as a consequence of the flow separation. Instabilities of this shear flow lead to the formation of vortical structures which induce free-surface distortions and grow in size while moving downstream.

The generation and the downstream propagation of free-surface fluctuations have been the subject of much research work, mostly in connection to breakers induced by submerged hydrofoils. Duncan & Dimas (1996), along with an analysis of the frequency spectrum decay of the free surface and of the velocity fluctuations, presented a careful study aimed at proving the shear-flow instabilities as the primary effect responsible for the free-surface fluctuations. The occurrence of free-surface fluctuations behind microbreakers is important in the interpretation of the radar backscatter when remote sensing is used for evaluating the free-surface state (Banner & Fooks 1985). Actually, the analytical model commonly adopted in deriving the free-surface elevation (Bragg model) may fail if the free-surface roughness exceeds its limit of applicability. An accurate analysis of this issue has been carried out by Walker *et al.* (1996) where free-surface measurements are used as an input for the Bragg model and the expected radar backscatter is evaluated and compared with the measured one. A detailed analysis has been also presented aimed at understanding the mechanisms governing the downstream propagation of the free-surface fluctuations. Wavenumber–frequency spectra indicate that the wavelength grows during their downstream motion while the temporal frequency of fluctuations, recorded at different longitudinal position, remains substantially constant. This led authors to speculate that the free-surface fluctuations behave like surface waves on a spatially varying current.

In the present paper, the unsteady wavy flow generated by a submerged hydrofoil starting from rest is simulated numerically. By varying the chord length of the hydrofoil, the relative importance of viscosity, gravity and surface tension is altered and a broad range of variation of some of the characteristic phenomena of unsteady breakers is modelled and studied. Several flow regimes are recovered, from plunging breaking down to very short spilling breaking wave. The action of the surface tension on the jet formation and on the entrapment of air is evaluated and the differences in the vorticity generation mechanisms are highlighted. At the smallest scale, the development of an intense shear flow arising from the toe is found, instabilities of which lead to the formation of coherent vortex structures that interact with the free surface giving rise to the downstream propagating fluctuations. Spectral analysis of the wave profiles is found to be in qualitative and quantitative agreement with the experimental results by Walker *et al.* (1996). Furthermore, details of the evolution of the coherent structures beneath the free surface show that secondary separations from the troughs of the free-surface fluctuations can occur as well.

The numerical approach is based on a two-dimensional unsteady Navier–Stokes solver for an incompressible two-fluid flow. In order to significantly reduce the computational effort, when simulating the wavy flow generated by a submerged hydrofoil, the domain decomposition approach developed in Iafrati & Campana (2003), is adopted. Although attention is mainly focused on the quasi-steady free-surface flow generated when the hydrofoil is moving with a constant speed, a sinusoidal ramp is used to accelerate the hydrofoil from rest with the aim of reducing the spurious free-surface fluctuations connected with the impulsive start. The air–water interface is captured by using a level-set approach (Sussman, Smereka & Osher 1994), thus allowing the description of free-surface flows even in the presence of complex interface topologies. The jump in the physical properties of the two fluids is spread across a small region about the interface. The surface tension contribution to the momentum equation is introduced by using the model originally suggested by Brackbill, Kothe & Zemach (1992) in the form of a continuum force obtained as the gradient of a smoothed Heaviside function. In this way, surface tension effects are spread on a narrow region about the interface.

The role played in terms of vorticity production by the thicknesses of the finite regions, along which jumps in fluid properties and surface tension effects are spread, is carefully evaluated in the case of a vortex dipole rising toward the free surface. For the purpose of validation, comparisons are established with results obtained by Ohring & Lugt (1991) through a surface fitting Navier–Stokes solver. This kind of vorticity–free-surface interaction is found to be particularly appropriate in this context since it exhibits strong similarities with the interaction, occurring behind microbreakers, between the downstream propagating coherent structures and the free surface.

2. Numerical model

2.1. *Domain decomposition technique*

The numerical description of free-surface flows can be challenging when changes in the interface topology take place. In the case of breaking waves, for instance, drops and air bubbles resulting from the plunging of the water jet onto the free surface need suitable numerical approaches to describe them accurately. In spite of the remarkable development of techniques able to handle complicated two-phase flows (see Scardovelli & Zaleski 1999 for a survey on the subject), the computational cost required by a detailed investigation of the breaking and post-breaking stages is still very high.

In the present study, attention is primarily focused on flow details occurring near the free surface while the hydrofoil is used only as a tool to generate waves. Hence, the use of a domain decomposition technique, with the adoption of the most appropriate model in different zones of the fluid domain, is helpful. Based on the above considerations, an unsteady heterogeneous domain decomposition approach has been developed for dealing with the wavy flow induced by a submerged hydrofoil in the presence of breaking (Iafrati & Campana 2003). A viscous model with an interface capturing technique is adopted in the free-surface region while, in the bottom region including the body, a potential flow approximation is used (see figure 1). A suitable coupling procedure is developed which allows the exchange of information between the sub-domains without overlapping.

In the bottom sub-domain Ω^B, the flow field is governed by a Laplace equation for the velocity potential φ which satisfies Neumann boundary conditions at inflow, outflow, bottom of the channel and all along the body contour. At the matching line, the velocity potential is assigned by integrating in time the unsteady Bernoulli equation:

$$\varphi = \int_0^t \left(\frac{\partial \varphi}{\partial t}\right) \mathrm{d}t = -\int_0^t \left(\frac{p^B}{\varrho} + g x_2 + \frac{|\boldsymbol{u}|^2}{2}\right) \mathrm{d}t, \qquad (2.1)$$

where ϱ is the fluid density, g is the acceleration due to gravity, x_2 is the vertical coordinate oriented upwards with $x_2 = 0$ at the still water level, $\boldsymbol{u}$ is the local fluid

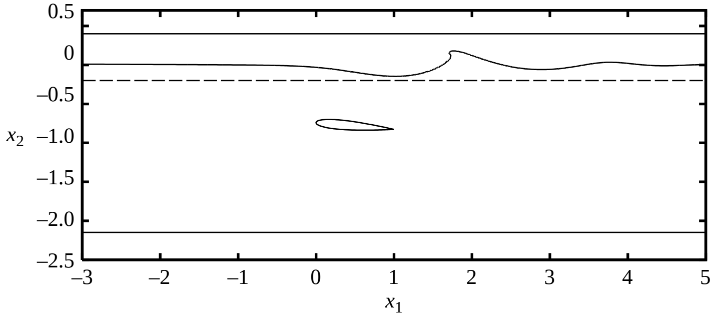

FIGURE 1. Sketch of the bottom and free surface sub-domains used for the domain decomposition approach. The body is moving from right to left beneath the air–water interface. The dashed line represents the matching line which separates the upper and lower sub-domains.

velocity and p^B is the pressure at the matching line evaluated as the limit from below.

Since normal stresses have to be continuous at the matching line Γ, the limit values from the lower and upper sub-domains must be equal. With the assumptions made for the flow in the lower sub-domain, only the pressure term p^B contributes to the limit from below, whereas the normal component of the viscous stresses has to be added to the pressure contribution when taking the limit value at the matching line from the upper sub-domain (Quarteroni & Valli 1999). Hence, by enforcing the matching between the two limit values it follows that

$$p^B = p - 2\mu \frac{\partial \boldsymbol{u} \cdot \boldsymbol{n}}{\partial n} \qquad \text{on } \Gamma, \tag{2.2}$$

$\boldsymbol{n}$ being the unit vector normal to the matching line, while μ and p are the fluid viscosity and the pressure field, respectively. The pressure p is that provided by the Navier–Stokes solver in the upper sub-domain.

The boundary-value problem is solved with the help of a boundary integral method which provides the normal derivative along the matching line. The latter and the velocity potential given by (2.1) determine the velocity field at the matching line which is used as a boundary condition along Γ when solving the Navier–Stokes equations in the upper sub-domain at the next time step.

In order to account for the circulation about the lifting body properly, a steady Kutta condition is enforced requiring that the fluid velocity at the trailing edge be directed along the hydrofoil mid-line. In the acceleration phase, during which the foil is accelerated from rest up to the final speed, the circulation about the hydrofoil is varying in time inducing shedding of vorticity that is not considered in the present model. This choice, which reduces the computational effort, is motivated by the fact that interest here is mainly concerned with the free-surface flow during the quasi-steady regime, that is in the later stage when the foil is moving with a constant speed and the shed of vorticity from the body is already ended. A more detailed discussion and validation of the coupling strategy is reported in Iafrati & Campana (2003).

2.2. *Navier–Stokes solver*

The two-phase flow of air and water is approximated as that of a single fluid with physical properties smoothly varying across the interface. By assuming the fluids to be incompressible, the continuity equation in generalized coordinates reads:

$$\frac{\partial U_m}{\partial \xi_m}=0, \tag{2.3}$$

where

$$U_m=J^{-1}\frac{\partial \xi_m}{\partial x_j}u_j \tag{2.4}$$

is the volume flux normal to the ξ_m iso-surface and J^{-1} is the inverse of the Jacobian.

Correspondingly, the momentum equation, in non-dimensional form, is

$$\begin{aligned}\frac{\partial}{\partial t}(J^{-1}u_i)+\frac{\partial}{\partial \xi_m}(U_m u_i)&=-\frac{1}{\varrho}\frac{\partial}{\partial \xi_m}\left(J^{-1}\frac{\partial \xi_m}{\partial x_i}p\right)-J^{-1}\frac{\delta_{i2}}{Fr^2}\\&-\frac{\kappa}{\varrho\, We^2}\frac{\partial}{\partial \xi_m}\left(J^{-1}\frac{\partial \xi_m}{\partial x_i}H_{\delta_T}(d)\right)+\frac{1}{\varrho\, Re}\frac{\partial}{\partial \xi_m}\left(\mu G^{ml}\frac{\partial u_i}{\partial \xi_l}+\mu B^{mlji}\frac{\partial u_j}{\partial \xi_l}\right),\end{aligned} \tag{2.5}$$

where u_i is the ith Cartesian velocity component, δ_{ij} is the Kronecker delta and

$$Fr=\frac{U_r}{\sqrt{gL_r}}, \qquad Re=\frac{U_r L_r \varrho_w}{\mu_w}, \qquad We=U_r\sqrt{\frac{\varrho_w L_r}{\sigma}} \tag{2.6}$$

are the Froude, Reynolds and Weber numbers, respectively. In (2.6), L_r and U_r are the chord of the hydrofoil and the towing speed, which are used as reference values for length and velocity, respectively, σ is the surface tension coefficient while ϱ_w, μ_w are the values of density and dynamic viscosity in water which are used as reference values for density ϱ and dynamic viscosity μ. In (2.5),

$$G^{ml}=J^{-1}\frac{\partial \xi_m}{\partial x_j}\frac{\partial \xi_l}{\partial x_j}, \qquad B^{mlji}=J^{-1}\frac{\partial \xi_m}{\partial x_j}\frac{\partial \xi_l}{\partial x_i} \tag{2.7}$$

are metric quantities and κ is the local curvature of the interface.

In order to avoid the introduction of surface forces, surface tension effects are modelled as a continuum force, by following the model originally suggested by Brackbill *et al.* (1992) and employed by Sussman & Puckett (2000). In the present model, the signed distance from the interface d, positive in water and negative in air, locates the interface. By introducing a smoothed Heaviside function

$$H_{\delta_T}(d)=\tfrac{1}{2}+\tfrac{1}{2}\sin\left(\frac{\pi d}{2\delta_T}\right) \text{ if } |d|<\delta_T, \tag{2.8}$$

with $H_{\delta_T}(d)=0$ if $d<-\delta_T$ and $H_{\delta_T}(d)=1$ if $d>\delta_T$, the surface tension forces are spread in a small neighbourhood, of thickness $2\delta_T$, about the interface.

The system of Navier–Stokes equations is discretized on a non-staggered grid as proposed by Zang, Street & Koseff (1994): Cartesian velocity components and pressure are defined at the cell centre, whereas volume fluxes are defined at the mid-point of the cell faces. A fractional step approach is employed: the momentum equation is first advanced in time by neglecting the pressure contribution (*predictor step*) which is successively reintroduced by enforcing the continuity of the velocity field (*corrector step*). The diagonal part of the dominating diffusive terms, i.e. that originated from $\nabla \boldsymbol{u}$, are computed with a Crank–Nicolson scheme, whereas all the other terms are computed explicitly through a three-step Runge–Kutta scheme (Rai & Moin 1991).

Apart from convective terms, which are discretized by a second-order upwind scheme (QUICK), the system of equations discussed above is spatially discretized by a second-order accurate central finite-difference. At each sub-step of the integration in time, the momentum equation is solved by using an approximate factorization of the diffusive part, as suggested by Kim & Moin (1985), for instance. For stability reasons, the time step is chosen so that the Courant number is always smaller than $\sqrt{3}$ and the constraint required by surface tension (Brackbill *et al.* 1992)

$$\Delta t < We\sqrt{\frac{(1+\varrho_a)}{4\pi}\Delta x_1^3},$$

is satisfied as well, with ϱ_a being the air density. Since not all the viscous contributions are treated implicitly, further limitations to the time step may be required.

A multigrid technique is adopted for the solution of the Poisson equation for the pressure correction, which is the most expensive part of the computational procedure. A corrector scheme is used for restriction and prolongation (Brandt 1992) and an LSOR method is employed as a high-frequency smoother. A simple average of the metric and of the distance function is used for deriving the coefficients of the discretized Poisson equation on the coarser grids. Additional details concerning the numerical solution of the Navier–Stokes equations are given in Iafrati & Campana (2003).

2.3. *Free surface capturing via a level-set technique*

The zero level of a function $d(\boldsymbol{x}, t)$ is used to capture the free-surface location (Sussman *et al.* 1994). At $t=0$, the function d is initialized as the signed normal distance from the interface, with $d>0$ in water, $d<0$ in air. Physical fluid properties are assumed to vary across the air–water interface according to the following equation:

$$f(d)=\begin{cases} f_a & \text{if } d<-\delta_P, \\ f_a+(f_w-f_a)H_{\delta_P}(d) & \text{if } |d|<\delta_P, \\ f_w & \text{if } d>\delta_P, \end{cases} \tag{2.9}$$

where the smoothed Heaviside function is given by (2.8) with the thickness δ_P used instead of δ_T. The parameter δ_P is the half-width of a smooth transition region which is needed to evaluate numerical derivatives appearing into the governing equations (Iafrati, Di Mascio & Campana 2001). During the motion, the function d is transported with the flow. The equation

$$\frac{\partial d}{\partial t}+\boldsymbol{u}\cdot\nabla d=0 \tag{2.10}$$

is integrated in time and the air–water interface is located as the level-set $d=0$. The integration in time is carried out with the three-step Runge–Kutta scheme by using the same discretization scheme as that adopted for the convective terms.

When simulating free-surface waves, disturbances propagate toward the upstream and downstream boundaries of the computational domain. In order to avoid spurious reflections from them, a numerical beach model is introduced in the transport equation (2.10)

$$\frac{\partial d}{\partial t}=-\boldsymbol{u}\cdot\nabla d-\nu(d+x_2). \tag{2.11}$$

The beach model (2.11) is applied to two regions close to the ends of the computational domain. The damping coefficient ν is zero at the inner limit of the beaches and grows quadratically toward the boundaries.

For fluid particles not lying on the free surface, the function d, initialized as the distance from the interface, loses its physical meaning during the motion, that is, for

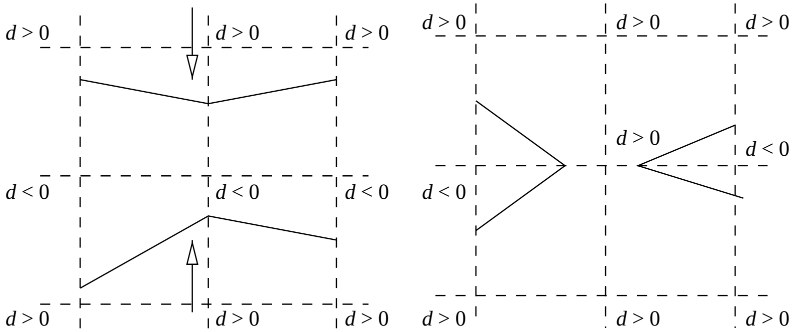

FIGURE 2. Sketch of the method adopted to locate the interface in the staggered grid. The two configurations indicate how the numerical technique deals with the changes in the interface topology.

the new configuration, the actual distance from the interface differs from the local value of the function d provided by integration of the transport (2.10). Hence, if the latter values were used in (2.9), the actual width of the transition region would become non-uniform along the interface and variable in time. In order to avoid this unwanted effect, the function d has to be reinitialized as the minimum (signed) distance from the interface.

From the numerical standpoint, as the distance function is defined at the cell centre, the system of staggered cells is considered and the interface passage within each of the staggered cells is easily recognized by the occurrence of a change in the sign of the distance function at two vertices. Once the interface passage within one staggered cell is identified, the intersection of the interface with the face of the staggered cell is found by linear interpolation of the distance values at the two corresponding vertices (see figure 2). It is worth remarking that, owing to the linear variation assumed for the distance function, only two or four intersections of the interface with the four faces of the staggered cell can be found, giving rise to one or two interface segments within each of the intersected cells (see Iafrati & Campana 2003 for additional details). Of course, owing to the linear variation assumed for the distance function within the staggered cells, the method adopted to locate the interface is only first-order accurate in space. The advantage of this assumption is that the interface portion lying within the cell is found without involving the distance values in the adjacent cells. The interface is represented in terms of a set of unconnected segments.

The occurrence of a change in the interface topology is easily managed by the adopted technique. It directly follows from the integration in time of the transport equation of the distance function (2.10). To explain how it works, in figure 2(*a*) two interface portions are shown along with the direction of the velocity field. Owing to the local gradient of the distance function and to the local velocity field, it happens that, after the numerical integration of the transport equation (2.10), the distance at the mid-point becomes positive, thus indicating that water is present. As a consequence, when the interface location is reconstructed on the basis of the new values of the distance function, the topology change appears.

About the reinitialization of the distance function, several efficient procedure have been developed by Russo & Smereka (2000) and Sussman & Fatemi (1999), among others. Varying from those procedures, in the present work, a direct reinitialization is used which consists in taking the minimum distance between cell centres and interface segments as reinitialized distance (Sussman & Dommermuth 2000). Attention being mainly focused on two-dimensional applications, the computational effort required by a direct reinitialization of the distance is not prohibitive (Iafrati & Campana 2003). For the sake of saving the computational effort, the reinitialization of the distance function is carried out only in a narrow band about the interface location and at the boundaries of the computational domain (Sethian 1999).

3. Numerical results

3.1. *Validation of the numerical method for the viscous interaction of two-dimensional vortices with a free surface*

Breaking waves generate a suite of processes that are among the most challenging for numerical methods. Direct numerical simulations of the Navier–Stokes equations for breaking waves have recently appeared in literature. In this framework, the use of fixed grid two-fluid methods, such as volume-of-fluid (Hirt & Nichols 1981; Lafaurie *et al.* 1994), particle tracers (Unverdi & Tryggvason 1992) or level-set (Sussman *et al.* 1994), able to describe the free-surface dynamics and to correctly capture the changes of the interface topology, has been the subject of much work.

The level-set technique, which is used here, has the ability to handle flows where the topology of the interface reaches great complexity. However, there are some concerns about the method's use of a finite thickness for the regions across which the jump of the fluid properties ($2\delta_P$) and the surface tension forces ($2\delta_T$) are spread. Since results presented in the following sections are primarily related to large-amplitude deformations generated by strong vortex–free-surface interaction, and owing to the strong assumptions made by the level-set approach about the interface, a validation step, through which the capability of the numerical procedure is carefully analysed, is deemed necessary. In particular, the purpose of the validation is twofold: verifying (i) the correct interaction of a vortex with the curved free surface, in particular in connection with the generation of secondary vorticity as a result of this interaction; and (ii) the capability of the continuum model to describe surface tension effects.

The validation is performed against the numerical results obtained by Ohring & Lugt (1991, hereinafter referred to as OL), who investigated the two-dimensional viscous interaction of a vortex pair with a deformable free surface, through a moving-grid approach. In that paper, only the flow field in the liquid phase is described via a boundary-fitted approach with exact boundary conditions directly applied at the sharp interface. A thorough discussion of the interaction of a viscous vortex pair with the free surface is provided when varying both the intensity of the ascending vortex pair and the free-surface compliance through several combinations of the Froude, Reynolds and Weber number values. It is shown that a secondary vorticity is generated as a result of the interaction of the primary vortex with the curved free surface. The influence of surface tension on the generation of secondary vorticity and on the paths of the primary vortices is investigated as well.

Bearing in mind the twofold scope of the comparison, two different flow conditions, without and with surface tension, are analysed. With the aim of investigating the role played by the grid resolution on the interface motion, two grid resolutions are employed (400×304 and 800×608) in a computational domain $-11 < x_1 < 11$, $-6 < x_2 < 6$. In the region where the interaction takes place, the coarse grid has a grid spacing comparable to that adopted in OL: $\Delta x_1 = \Delta x_2 = 0.02$. Outside this region ($|x_1| > 3$, $x_2 > 0.5$ and $x_2 < -4$), grid spacing is gradually increased. The initial velocity distribution is assigned according to Lamb's formula for the decaying vortex. More details concerning initial and boundary conditions are reported in OL and are not repeated here. It is worth recalling that definitions of the non-dimensional parameters in OL differ from those adopted here and then, in the following, their values are denoted by the superscript OL. In particular, the initial distance of the vortex centres is used as the reference value for length, the initial translation velocity of the dipole is used as the reference value for the velocity and, moreover, the Weber number in OL is defined as

$$We^{OL} = \frac{\sigma}{\varrho_w L_r U_r^2}.$$

The validation is carried out by using the full Navier–Stokes solver in the whole fluid domain while the validation of the domain decomposition approach is the subject of the next section. Since the present method deals with a two-fluid flow, density and viscosity ratios between the two fluids are assumed as the real ones as for air and water.

In figure 3, the evolution of the vorticity contours is shown for the two grids in the case $Re^{OL} = 100$, $Fr^{OL} = 0.2$, $We^{OL} = 0$. In both cases, $\delta_P = 0.05$ is used, which means that five and ten grid cells are within the transition region in the coarse and fine grid computations, respectively. From the time sequence, a striking similarity with results obtained by OL can be observed. Looking at the configurations at $t = 3.5$, even though the free surface at the mid-line $x_1 = 0$ is only slightly raised, a sharp depression, called a ‘scar’, appears as a result of the interaction with the primary vortex. The flow behind the scar is unable to follow the sharp curvature, causing the formation of secondary (counter-clockwise) vorticity. At a later stage ($t = 6.5$), the primary vorticity (negative on this side of the fluid domain) leads to the detachment of a weak secondary vortex, which swings around the primary one, leaving behind a weak tongue of positive vorticity. At least on the fine grid, the occurrence of a small region of positive vorticity still attached to the free surface can also be recognized. As discussed below, although this region is almost entirely inside the transition region adopted for the fluid properties, a very good agreement with the results reported in OL is achieved.

The comparison between the two sequences in figure 3 show that the evolution of the vorticity field is essentially the same on both grids. The most relevant difference is that the results provided by the coarse grid slightly underestimate the generation of secondary vorticity, missing the highest positive vorticity contour ($\omega = +0.45$) at $t = 6.5$.

In order to investigate this point, the dissipation rate of the primary vortex has been evaluated and compared with the theoretical law given by Lamb, as done in OL. Both grids predict the vorticity decay with good agreement (see figure 4*a*), at least up to $t \simeq 6$ when the viscous interaction with the free surface begins to matter, thus indicating that the coarser grid is sufficiently refined to provide a correct vorticity diffusion. Hence, it is here conjectured that the small number of cells distributed within the transition region prevents the coarse grid computation describing the interaction between vorticity and free surface with the same accuracy provided by the finer one. Further comparisons have been established in terms of the path of the vorticity peaks and of the free-surface elevation at $x_1 = 0$. The two grids provide nearly identical results, not shown, with differences always smaller than the cell size.

Mass conservation properties are evaluated in terms of the total non-dimensional mass M, defined as

$$M = A_w + A_a \varrho_a / \varrho_w,$$

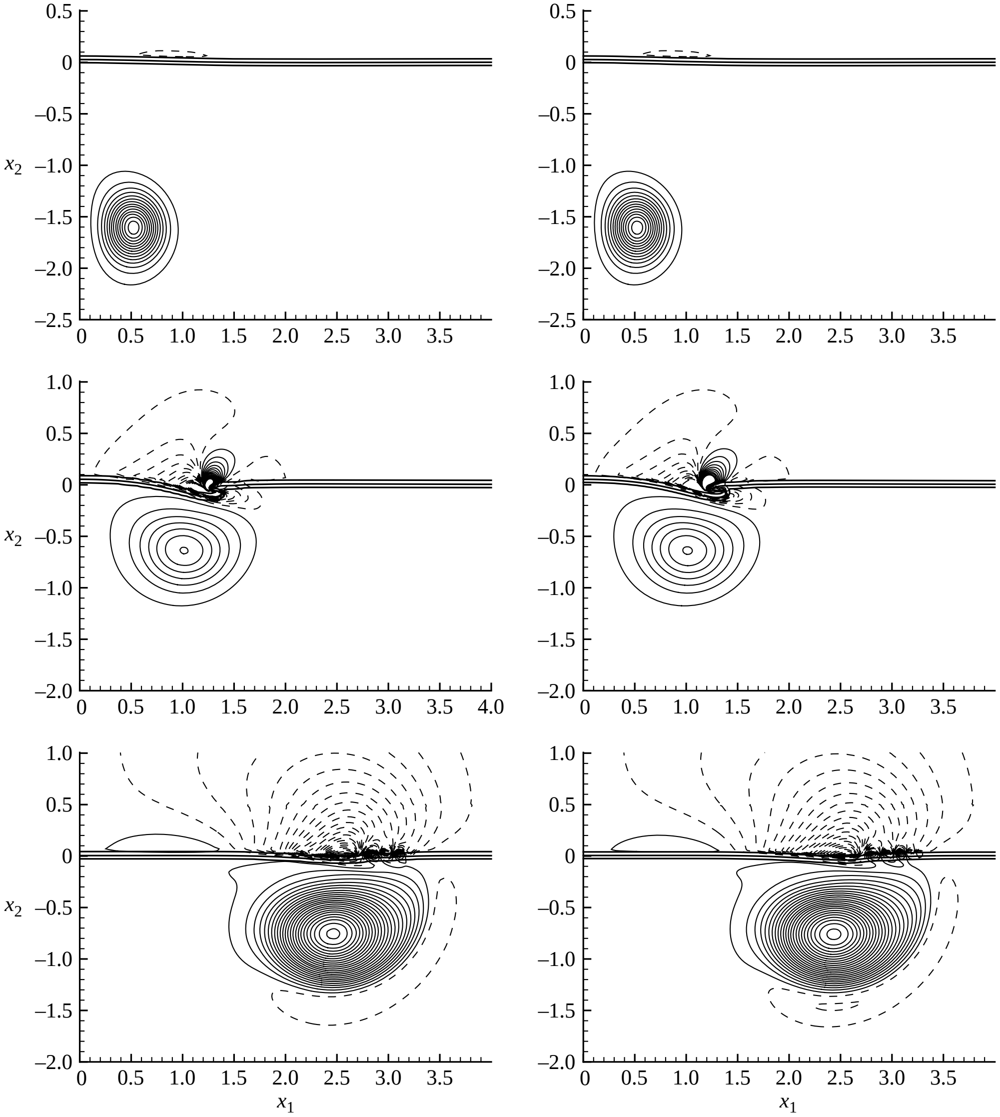

FIGURE 3. Vorticity contours (dashed line for positive vorticity) for dipole–free-surface interaction without surface tension effects: $Re^{OL} = 100$, $Fr^{OL} = 0.2$ and $We^{OL} = 0$. Results for coarse and fine grid resolutions are shown in the left-hand and right-hand columns, respectively. From top to bottom, configurations refer to time $t = 1.5, 3.5, 6.5$. According to results shown in Ohring & Lugt (1991), vorticity contours are $\ldots, -3, -1, +1, +3, \ldots$ for $t = 1.5, 3.5$ and $\ldots, -0.45, -0.15, +0.15, +0.45, \ldots$ for $t = 6.5$. To highlight the extension of the transition region used for the physical properties, three density contours ($\varrho = 0.03, 0.50, 0.95$) are plotted with thicker lines.

where A_w and A_a denote the area of the water and air sub-domains, respectively. The value of M divided by the corresponding initial value M_0 is plotted versus time in figure 4(b), showing that the mass variation is always a very small fraction of the initial value, being $7 \times 10^{-4}\ M_0$ and $5 \times 10^{-4}\ M_0$ for the coarse and fine grid, respectively. In both calculations, an abrupt variation takes place about $t = 3.5$ when

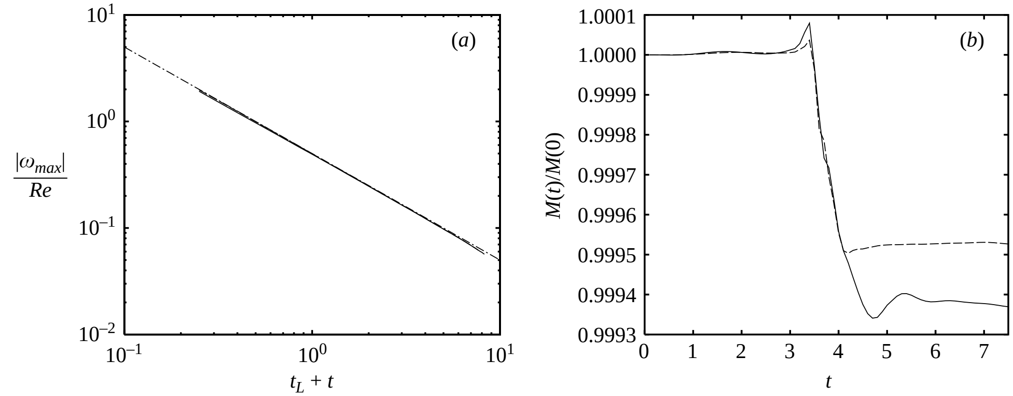

FIGURE 4. Effect of the grid resolution on the maximum of vorticity (ω_{max}) and on the mass conservation $M(t)/M(0)$. Coarse and fine grid results are shown with solid and dashed lines, respectively. Lamb's law for the decaying vortex is also reported with a dash-dotted line in (*a*).

a intense vorticity–free-surface interaction takes place and the interface undergoes a strong deformation (see figure 3).

With regard to the use of a finite thickness for the transition of the fluid properties, the results obtained seem essentially unaffected by this assumption of the numerical model. At $t = 3.5$, the difference between the maximum and the minimum free-surface elevation is about 0.18, which appears rather small compared to the thickness of the transition region $2\delta_P = 0.1$. This large value of δ_P is required in order to have at least five points within the transition region when using the coarse grid. In spite of the rather large transition region, in comparison to the free-surface deformations, a good agreement with OL is achieved. Hence, concerning the first of the two purposes of the validation, provided that a reasonably large number of grid cells are inside the transition region, the spreading of the fluid properties across a finite region about the interface does not prevent a reasonably accurate prediction of the free-surface dynamics and of its interaction with the vorticity field.

In order to evaluate the capability of the numerical model to describe surface tension effects correctly, another case, among those presented by OL, is considered for which $Re^{OL} = 100$, $Fr^{OL} = 0.4$ and $We^{OL} = 1$. With respect to the previous case, the rising speed of the primary vortex is doubled, but, in this case, surface tension plays a relevant role in reducing the deformation of the free surface and, in turn, the production of secondary vorticity. Two numerical computations are carried out by using the finer grid with surface tension forces spread across regions of different extensions: $\delta_T = 0.05$ and $\delta_T = 0.025$. Results at three time instants, displayed in figure 5, do not exhibit substantial changes in terms of the primary vortex evolution. However, by comparing the vorticity fields at $t = 5.0$, it can be seen that for $\delta_T = 0.05$, the contour $\omega = +1$ in the water domain is lost. For $\delta_T = 0.025$, results are much closer to those reported in OL, although the vorticity contour at $\omega = +1$ is still slightly smaller.

On the basis of the above considerations, it follows that, for correct evaluation of their effects, surface tension forces ought not be spread across a region that is too wide compared to the local radius of curvature of the interface. Conversely, the thickness of this region cannot be smaller than, say, five grid cells in order to ensure a correct evaluation of the interface curvature through numerical differentiation of the smoothed Heaviside function (2.8).

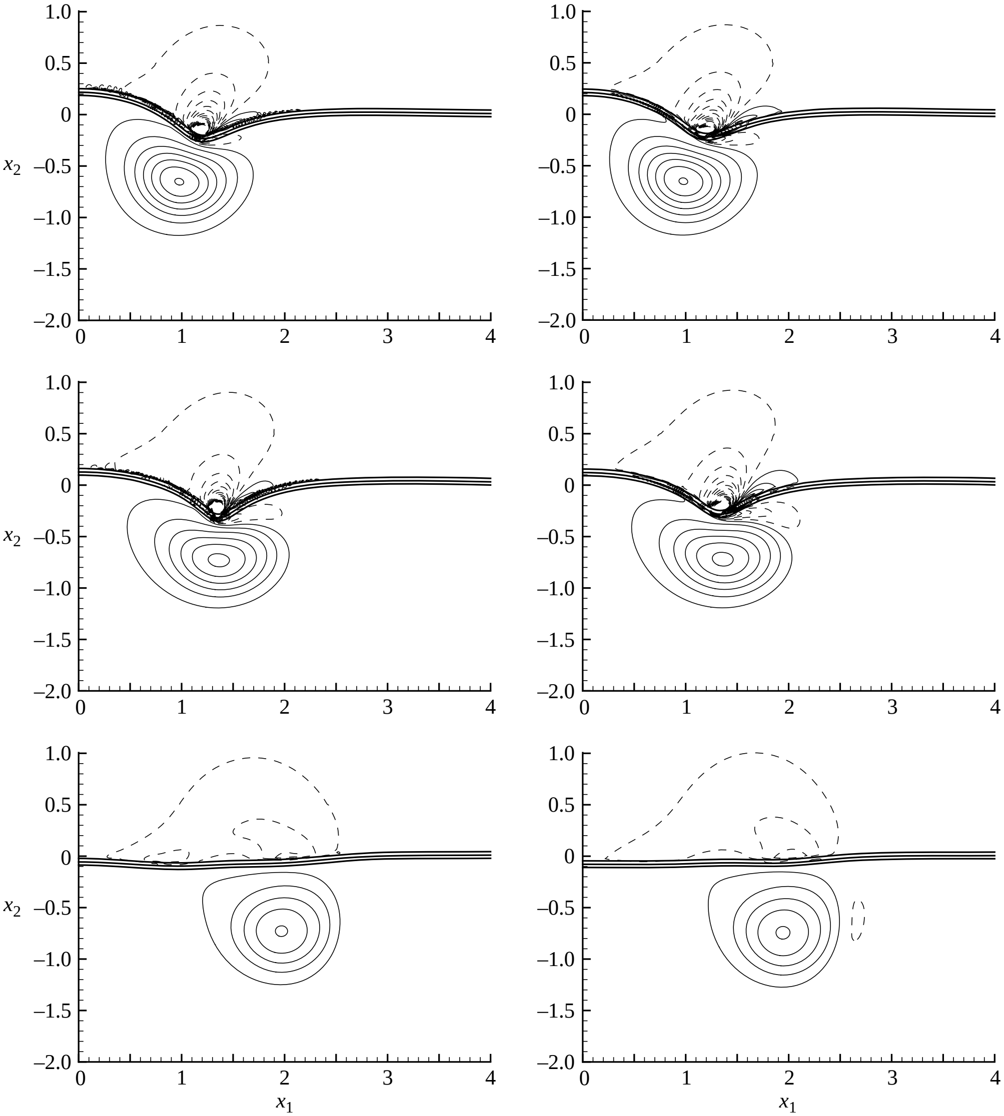

FIGURE 5. Vorticity contours for dipole–free-surface interaction with surface tension effects: $Re^{OL} = 100$, $Fr^{OL} = 0.4$ and $We^{OL} = 1$. Left-hand and right-hand columns refer to the cases $\delta_T = \delta_P = 0.05$ and $\delta_T = \delta_P/2 = 0.025$, respectively. Both calculations are performed on the fine grid. From top to bottom, configurations at times $t = 3.5, 4.0, 5.0$ are shown. As in Ohring & Lugt (1991), vorticity contours are $\ldots, -3, -1, +1, +3, \ldots$. To highlight the extension of the transition region for physical properties, three density contours ($\varrho = 0.03, 0.50, 0.95$) are plotted with thicker lines.

In the following, numerical calculations are always carried out by assuming $\delta_P = \delta_T$. The reason is that, owing to the large extension of the computational domain in the horizontal direction, the cell size is increased when moving from the (central) breaking region towards the upstream and downstream boundaries. Hence, δ_P and δ_T are chosen as the smallest values (about 2.5 grid cells) that allow reasonably accurate results to be obtained throughout the computational domain, even in those regions where the largest cell size is used. Starting from this small value, a further reduction of δ_T is not advisable.

3.2. *Validation of the domain decomposition approach in the case of a regular wavetrain generated by a submerged hydrofoil*

With the aim of validating the domain decomposition approach, the numerical model is used for simulating the free-surface flow generated by a NACA 0012 hydrofoil moving beneath the interface at an angle of attack $\alpha = 5^\circ$. The hydrofoil is initially at rest under a flat free surface located at $x_2 = 0$ and is gradually accelerated with a sinusoidal ramp up to the final speed in a time $t = t^R$. The chord of the hydrofoil L_r is used as the reference value for lengths, the final speed U_r is used as the reference value for velocities and their ratio $T_r = L_r/U_r$ is used as the reference value for time. It is worth noting that, in all the simulations presented in the following, the viscosity and density ratios are assumed to be equal to the real ones for air and water.

On the basis of the experimental conditions used in Duncan (1983), the hydrofoil has a chord of 20.30 cm and is towed at 80 cm s^{-1}, which corresponds to a Froude number $Fr = 0.567$. At this Froude number, a regular wavy flow has been experimentally found when using a non-dimensional submergence at a quarter of the chord $h_s = 1.285$. The Weber number is assumed equal to the experimental one, $We = 42.20$, while a smaller Reynolds number, $Re = 10\,000$, is used in the numerical calculations. As important viscous effects are not expected in the free-surface region for this calculation, such a high Reynolds number does not pose any problem concerning the grid resolution.

In a frame of reference attached to the body, the computational domain horizontally spans from $x_1 = -15$ to $x_1 = 15$. Before the rotation, the hydrofoil is between $x_1 = 0$ and $x_1 = 1$ (see figure 1). Then it is rotated clockwise about a quarter of the chord of an angle $\alpha = 5^\circ$. In this frame of reference, a uniform velocity profile $\boldsymbol{u} = (U(t), 0)$ is applied on the upstream and downstream boundaries, where $U(t)$ is the non-dimensional velocity of the hydrofoil and is given by

$$U(t) = \begin{cases} \frac{1}{2}\sin\left[\pi\left(\dfrac{t}{t_R} - 0.5\right)\right] + \frac{1}{2}, & t < t_R, \\ 1, & t \geqslant t_R. \end{cases} \tag{3.1}$$

For the present calculation, in order to make smoother the achievement of a steady solution, a long acceleration ramp ($t^R = 50$) is used. In the vertical direction, the upper sub-domain extends from $x_2 = -0.2$ to $x_2 = 0.4$ whereas the domain Ω^B extends from $x_2 = -2.1477$ (the bottom of the channel) up to $x_2 = -0.2$ (the matching line). On the top boundary, $x_2 = 0.4$, a uniform velocity profile $\boldsymbol{u} = (U(t), 0)$ is assigned, with $U(t)$ given by (3.1). Numerical beaches (2.11) are placed at both the sides of the domain, that is for $x_1 \in (-15, -8)$ and $x_1 \in (8, 15)$. The damping coefficient of the beach model takes its maximum value $\nu = 3$ at the two ends of the computational domain.

In figure 6, the free-surface profile obtained at $t = 100$ by the unsteady domain decomposition approach is compared with an inviscid fully nonlinear solution, with a finite-volume solution of the Reynolds averaged Navier–Stokes equations (RANS) (Muscari & Di Mascio 2003) and with the experimental data obtained by Duncan (1983). The comparison shows that the domain decomposition approach provides a satisfactory result which is in good agreement with the fully nonlinear inviscid solution and with the experimental data. Concerning the gains from using the domain decomposition approach, the efficiency stems from the smallness of the (vertical) portion of the whole computational domain (about a quarter) where the more expensive viscous flow solver is employed. Deeper validation tests and further details

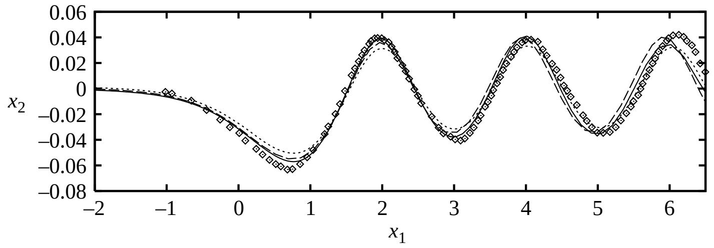

FIGURE 6. Regular wavy flow past a towed hydrofoil. Results obtained by —, domain decomposition are compared with - - -, those obtained by a fully nonlinear boundary element solver, . . . , a RANS model and ◇, experimental data. The chord of the hydrofoil is used as a reference value for lengths, leading to a non-dimensional wavelength $\lambda_\infty = 2.02$.

L_r (cm)	U_r (cm s^{-1})	Re^{fs}	We
20.300	80.00	162400	42.20
10.150	56.57	57417	21.10
5.075	40.00	20300	10.55

TABLE 1. Non-dimensional parameters of hypothetical full-scale experiments at several values of the chord of the hydrofoil L_r and towing speed U_r.

of the unsteady domain decomposition approach are discussed in Iafrati & Campana (2003).

3.3. *Scale effects on wave breaking onset*

In order to study the unsteady flow generated by the breaking wave, the experimental observations by Duncan (1981) are followed and the non-dimensional submergence of the hydrofoil is reduced to the value $h_s = 0.783$. With the aim of resolving flow details taking place in the breaking region, a locally refined grid is adopted with a minimum grid spacing $\Delta x_1 = 0.0027$ and $\Delta x_2 = 0.0025$, thus resulting in a grid of 768×192 points for the upper sub-domain. The thickness of the transition region is reduced correspondingly. Surface tension forces and jumps in the fluid properties are spread across a stripe with a half-thickness of $\delta_T = \delta_P = 0.02$. Initial and boundary conditions are essentially the same as those used in the previous section. The only difference is the duration of the acceleration ramp which is now reduced to $t^R = 10$ units of time, since a steady solution is not expected for this hydrofoil's submergence.

In order to analyse the role played by the surface tension when the length scale is progressively reduced, three different numerical simulations are performed by keeping constant the Froude and Reynolds numbers ($Fr = 0.567$ and $Re = 1000$) and halving twice the Weber number, starting from the full-scale value in Duncan's experiments. From (2.6), as the Weber number is varying by keeping constant the Froude number, it follows that

$$We = Fr\, L_r \sqrt{\frac{\varrho_w g}{\sigma}}, \tag{3.2}$$

which implies that halving the Weber number experimentally would correspond to halving the chord of the hydrofoil L_r (see table 1).

In figure 7, three different stages of the breaking wave establishment for the case $We = 42.20$ are shown in terms of vorticity and density contours. This condition corresponds to a hydrofoil with chord 20.30 cm towed at 80 cm s^{-1} (table 1), and the

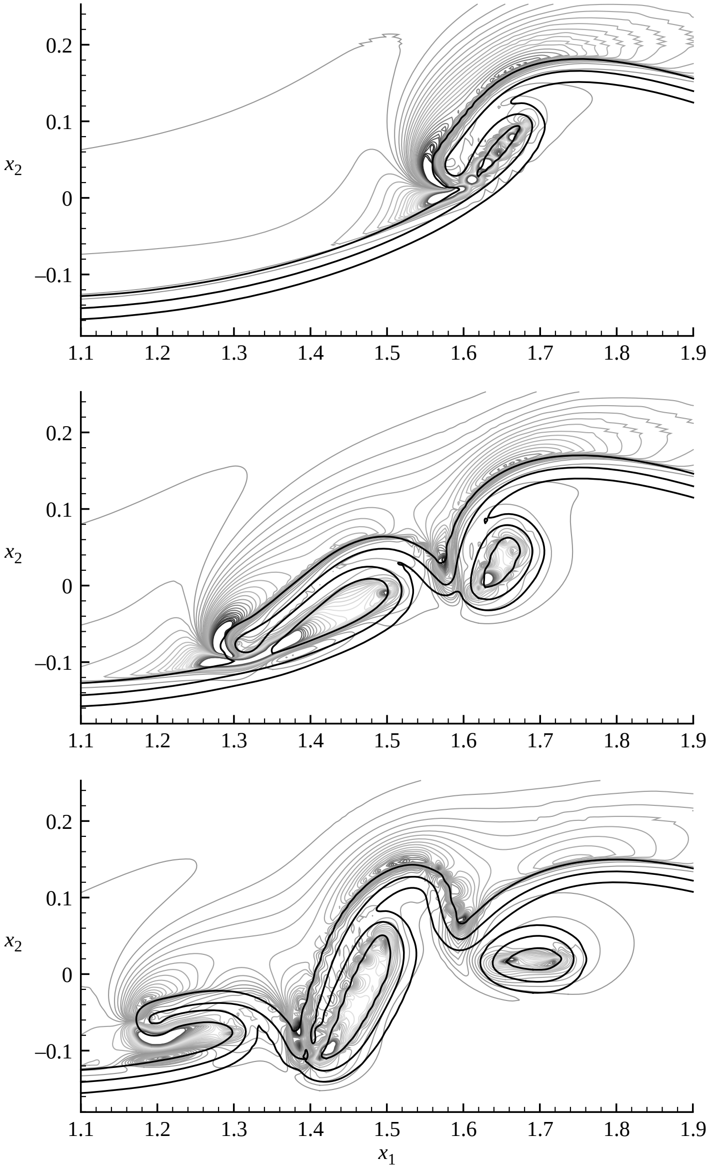

FIGURE 7. Vorticity contours at three different stages of the wave-breaking establishment for the case $We = 42.20$. Thicker lines represent density contours at $\varrho = 0.03, 0.50, 0.95$, respectively. From top to bottom $t = 13.8, 14.2, 14.4$. Reference values for length and time are 20.30 cm and 0.2537 s, respectively.

reference value for time is $T_r = 0.2537$ s. It is worth noting that, owing to the baroclinic contribution, the behaviour of the vorticity contours within the transition region can be somewhat misleading. Hence, beside the mean density level, two density contours are also plotted to bound the transition region.

At such a Weber number, surface tension is not yet able to prevent the wave overturning and the jet formation at the crest, but it is already strong enough to round the tip of the jet as a consequence of the large curvature values (Tulin 1996). This jet propagates upstream and impacts on the free surface, giving rise to the

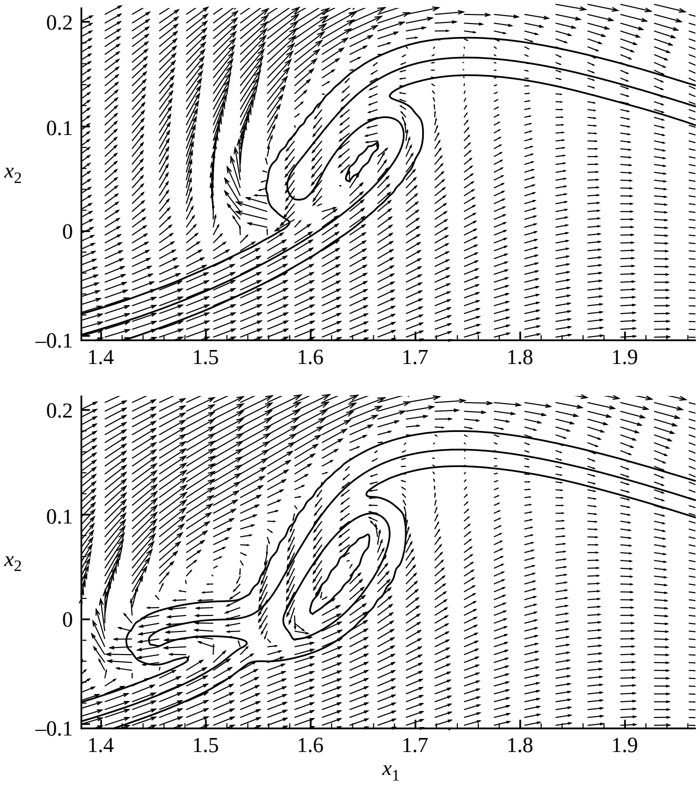

FIGURE 8. Velocity field in air and water at two different stages of the free-surface reconnection process ($We = 42.20$). From top to bottom $t = 13.8, 14.0$. Thicker lines represent density contours at $\varrho = 0.03, 0.50, 0.95$, respectively. For clarity, only one in every three velocity vectors is drawn.

formation of a new jet (figure 7, $t = 14.2$). Depending on the violence of the first jet impact, several splash-up cycles may take place (Bonmarin 1989), see figure 7, $t = 14.4$.

A careful observation of the sequence in figure 7 reveals that strong interactions take place between the plunging jets and the underlying water surface even before the mid-density lines, representing the interface, are in contact. Aside from the obvious numerical effects related to the spreading of the density jump onto a finite region, it has to be noted that the two-dimensional assumption allows the escape of the air only upstream. On the contrary, in a real three-dimensional flow, any transversal fluctuation greatly helps the air to escape in any direction. In spite of the interest of this point, a deeper investigation is out of the scope of the present paper which is mainly concerned with the description of breaking waves when surface tension is strong enough to prevent air entrainment.

In a recent numerical study by Chen *et al.* (1999), a close-up view of the velocity field in the splashing region shows that, at the initial stage of the impact, the liquid in the new developing jet is mainly composed of fluid coming from the jet itself. A similar consideration can also be drawn on the basis of the present results, although a careful inspection of the velocity field reveals a more complicated time-dependent behaviour. At the beginning of the impact, the jet seems to rebound from the free-surface split into two opposite branches, with the largest one almost entirely flowing toward the new jet (figure 8, $t = 13.8$). At a later stage (figure 8, $t = 14.0$), the impinging jet penetrates deeply into the free surface and pushes the upper layer of the incoming current to flow into the developing jet. These two conditions correspond to the two extreme modes of slash-up discussed in Peregrine (1983); present results indicates that these two extreme modes take place at different stages of the jet impact process.

As a consequence of the jet impact after wave overturning, the fluid domain changes from simply connected to doubly or multiply connected, with a significant amount of circulation around the cavities (see figure 8, $t = 14.0$). The impulsive generation of circulation originated by the free-surface reconnection is an essentially inviscid mechanism and fluid viscosity does not play a significant role on this respect. This important mechanism for generation of circulation has been investigated by Best (1993) and by Zhang, Duncan & Chahine (1993) in the framework of the re-entrant jet impact on collapsing cavitation bubbles. In Battjes (1988) and Tulin (1996), the same effect is discussed in the context of the breaking waves. On the basis of the present numerical results, the marginal role played by viscosity in this process is further confirmed by the small amount of vorticity spread about the cavity (see figure 7, $t = 14.2, 14.4$), in spite of the low Reynolds number.

When reducing the length scale, the increasing surface tension effect progressively changes the mechanism governing the breaking-wave establishment, gradually reducing the intensity of the jet and the amount of air entrapped. For a Weber number $We = 21.10$, which corresponds to a hydrofoil chord of 10.15 cm, towing speed of $56.57\,\mathrm{cm\,s^{-1}}$ (table 1) and $T_r = 0.1794\,\mathrm{s}$, it can be noted that a jet is still present, but it is much slower and the subsequent impact on the free surface is much milder than that found for $We = 42.20$. Furthermore, by looking at the vorticity contours, instead of a violent impact, the jet appears to slide down carrying a whole body of water, thus giving rise to a shear-layer development starting from the jet root.

A careful observation of figure 9 reveals that the shear layer develops although there is no contact with the middle density level. This means that it is the result of the viscous interaction between two fluid layers which have density values larger than air, but smaller that the middle density layer and move in opposite directions. Of course, it would be significantly different if pure water layers were interacting.

A further halving of the length scale leads to the entire suppression of the jet formation and of the air entrapment, as is shown by the sequence in figure 10. The chord of the hydrofoil is 5.075 cm, the towing speed is $40\,\mathrm{cm\,s^{-1}}$ and $T_r = 0.1269\,\mathrm{s}$. In this case, after the wave steepening, a bulge grows up about the crest until its weight drives the body of water to slide down upon the forward face of the wave. During the downslope motion of the bulge, a flow separation takes place at the toe and a strong shear flow develops between the fluid into the bulge and the upslope flow incoming from upstream. This shear flow rapidly propagates downstream, remaining close to the free surface.

With the aim understanding better the free-surface evolution in this surface tension dominated breaking wave, the time history of the free-surface profile for a long time simulation is shown in figure 11. A vertical shift corresponding to the time delay is applied among successive profiles for the sake of clarity. This sequence clearly displays the initial wave steepening and subsequent bulge development. As time elapses, the bulge slides down and, after reaching the foremost position, experiences a damped oscillatory motion in the horizontal direction with a regular period.

Oscillations of the breaker toe have been experimentally observed by Duncan (1981), Lin & Rockwell (1995) and Walker *et al.* (1996). In Duncan (1981), the period of the breaker toe oscillations T^{BT} is found to be about 4.4 times the period

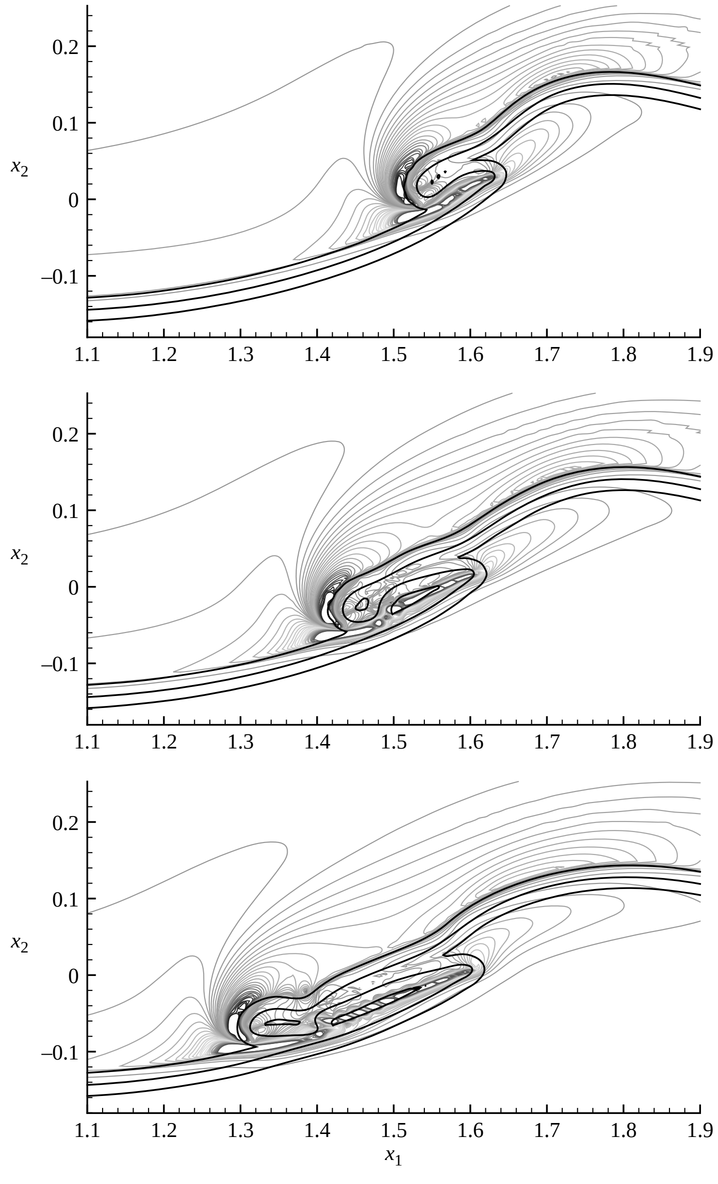

FIGURE 9. Vorticity contours at three different stages of the wave-breaking establishment for the case $We = 21.10$. From top to bottom $t = 13.8$, 14.0, 14.2. Reference values for length and time are 10.15 cm and 0.1794 s, respectively.

of the following waves T_∞. This led Duncan to speculate that these low-frequency oscillations are due to the wave components generated when the foil is started from rest. As these wave components have a group velocity equal to the hydrofoil speed, by linear theory their period is $4T_\infty$. In Lin & Rockwell (1995), the ratio T^{BT}/T_∞ is measured in the range 4.89 to 6.12. In Walker *et al.* (1996), the low-frequency component of the free-surface fluctuations is found to be about 2.95 rad s^{-1} which corresponds to a period $T^{BT} = 2.13$ s, that is $T^{BT}/T_\infty = 3.08$.

Concerning the numerical results, from figure 11, it can be seen that the breaker toe oscillates with a period which is about $T^{BT} = 8.25$ units of time compared with the

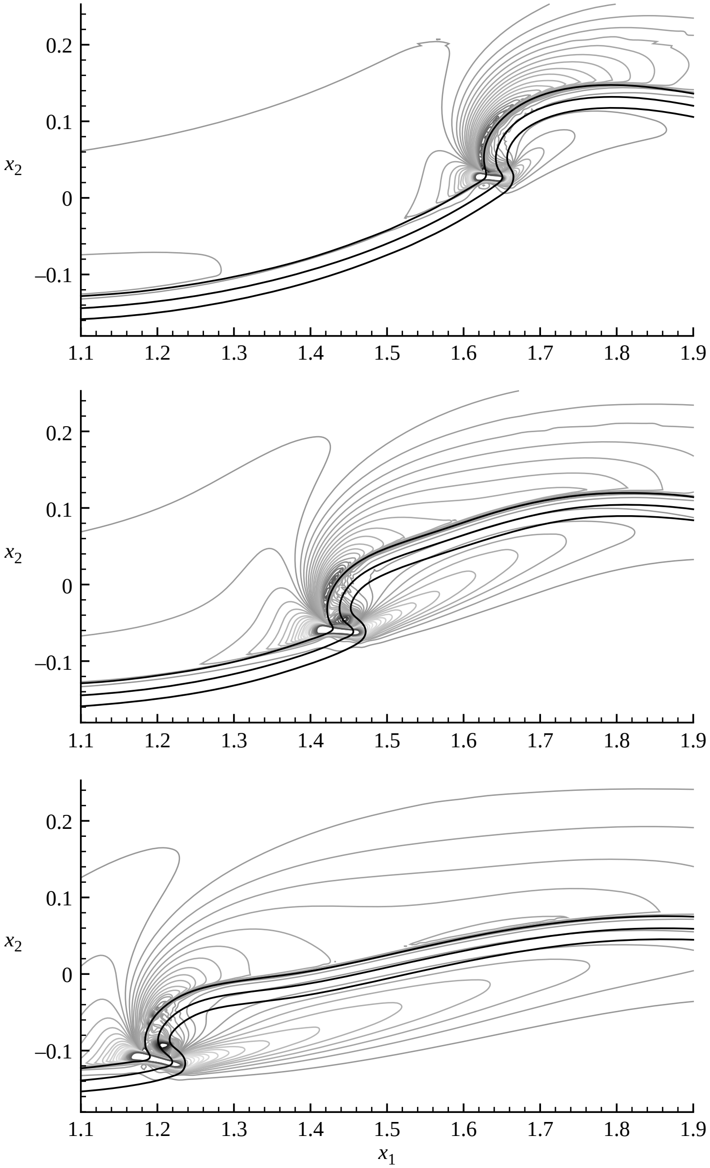

FIGURE 10. Vorticity contours at three different stages of the wave-breaking establishment for the case $We = 10.55$. From top to bottom $t = 12.7, 13.7, 14.7$. Reference values for length and time are 5.075 cm and 0.1269 s, respectively.

period of the following waves $T_\infty = 2\pi Fr^2/U_\infty = 2.02$. From these data, it follows that $T^{BT}/T_\infty = 4.08$, a value that is within the range 3.08 to 6.12 experimentally measured.

3.4. *Downstream-propagating free-surface fluctuations behind microbreakers*

A more refined analysis of the profile history highlights some phenomena in the free-surface evolution. Although the damped oscillatory motion appears smooth and the free-surface profiles are highly regular, a closer inspection, shown in figure 12, reveals the presence of small downstream-propagating surface fluctuations. Numerical results show that these fluctuations are periodically induced on the free surface each time the

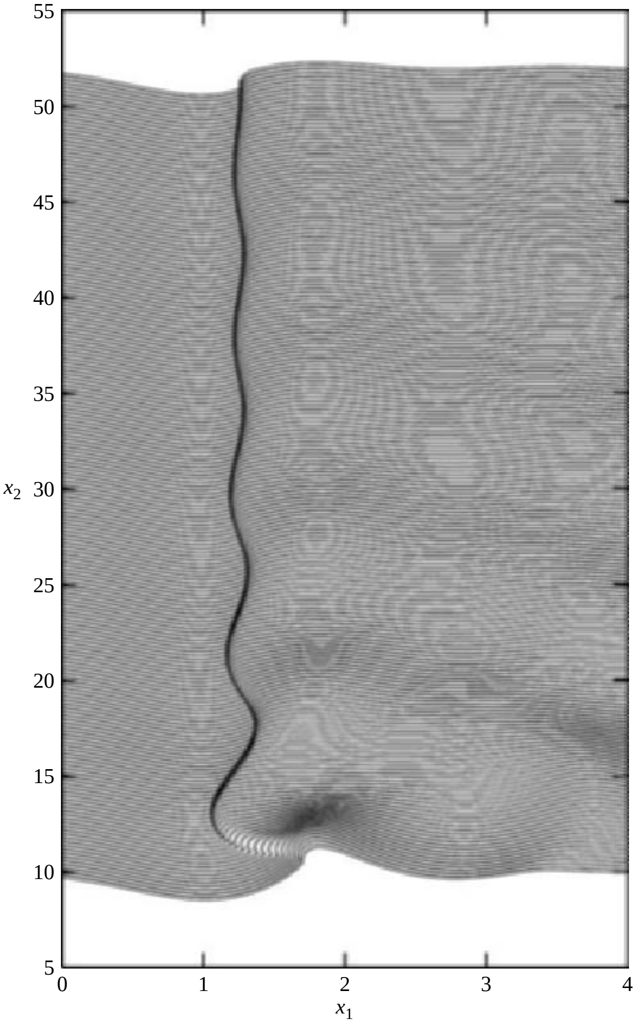

FIGURE 11. Time sequence of the free-surface profiles for the case $We = 10.55$ and $Re = 1000$. The time step between two successive profiles is $\Delta t = 0.2$. A vertical shift corresponding to the actual time is applied at each free-surface configuration. For clarity, the free-surface elevation is multiplied by a scale factor 10.

toe experiences its downslope motion, even though their amplitude diminishes from time to time owing to the damped motion of the toe.

In order to investigate the nature of these fluctuations and the effects of the Reynolds number on their generation mechanism, the same numerical simulation is repeated at a higher Reynolds number, $Re = 2500$. Note that this value is still significantly smaller than the experimental values used in Duncan & Dimas (1996) and in Walker *et al.* (1996), as reported in table 2. The resulting profile history, shown in figure 13, clearly displays much larger free-surface fluctuations propagating downstream with respect to those found in the case $Re = 1000$. At this Reynolds number, free-surface fluctuations are generated independently of the toe motion, with recurrence even when the toe is at rest or is experiencing an upslope motion. Moreover, the first downslope motion of the bulge is much faster and pushes the

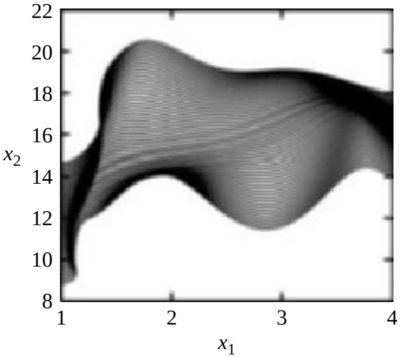

FIGURE 12. Here a detailed view of the time sequence in figure 11 is shown to highlight the presence of downstream propagating fluctuations on the free surface. In this case, the time step between two successive profiles is $\Delta t = 0.1$ and the scale factor is 30.

	Fr	*We*	*Re*	Foil type
Walker *et al.*	0.625	69.70	328320.	NACA 0015
Coakley & Duncan	0.571	31.40 − 62.81	103920 ÷ 293940	NACA 0012
Duncan & Dimas	0.45 − 0.75	29.92 − 49.87	108840 ÷ 181400	FX 63 − 137
Present calculations	0.567	10.55	2500	NACA 0012

TABLE 2. Flow conditions used in Walker *et al.* (1996), in Coakley & Duncan (1996), in Duncan & Dimas (1996) and in the present numerical simulation.

toe further upstream. Finally, the subsequent oscillatory motion of the bulge appears more irregular and its amplitude is damped more rapidly.

While an accurate description of the mechanisms responsible for the free-surface fluctuations is postponed to the next section, where the flow field beneath them is carefully analysed, in the following, the initial growth and the downstream propagation are investigated on the basis of the free-surface profiles.

Figures 11 and 13 show a lack of capillary ripples in front of the bulge. Although, as experimentally proved by Lin & Rockwell (1995), the capillary pattern is strongly dependent on the Froude number, with small speed variations capable of reducing, or even suppressing, the capillary wavetrain, we suspect that this lack in the numerical results might be related to the thickness of the transition region. Hence, with the aim of evaluating the limitations intrinsic to the use of such a numerical approach, another simulation is carried out by using a halved value of thickness parameters $\delta_T = \delta_P = 0.01$, and comparisons are established with the previous results. In figure 14, a sequence of free-surface configurations at several stages of the wave-breaking development is presented, showing that the use of a smaller thickness of the transition region leads to the formation of a small-scale capillary pattern in front of the bulge which, however, disappears during the fast downslope motion of the bulge. From a close-up view (not shown) of the free-surface profiles obtained in the case $\delta_T = \delta_P = 0.01$, two small capillary ripples can be identified having amplitudes 0.007 and 0.003 and wavelengths of about 0.05 and 0.0375. The fact that they disappear when using a wider transition region has to be ascribed to the limit that the adopted model has in describing waves of amplitude comparable to the thickness of the region along which the density jump is spread.

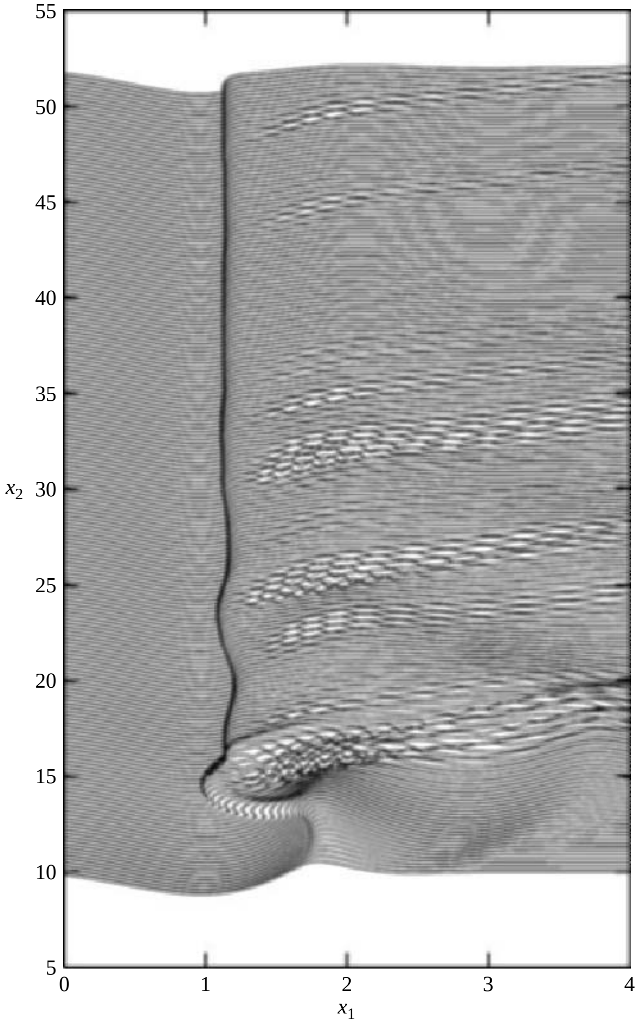

FIGURE 13. Time sequence of the free-surface profiles for the case $We = 10.55$ and $Re = 2500$. Time step and scale factor are the same as adopted for figure 11.

Aside from a faster downslope motion of the bulge, the sequence obtained for smaller δ_T and δ_P does not display a significant change in terms of the long time evolution. In order to justify the last statement, free-surface profiles obtained by using the two different thicknesses of the transition regions are compared at a later stage, when free-surface fluctuations are fully developed (figure 15). In drawing the graph, the faster dynamics characterizing the simulation with the smaller thickness of the transition regions has been accounted for, so that the two profiles do not refer to the same time instant. The comparison indicates that, but for a phase shift in their generation, no differences occur in terms of amplitude and wavelength of the fluctuations. From figure 15 the size of the free-surface fluctuations can also be evaluated. The crest-to-trough amplitude of the fluctuations is about 0.09 and their wavelength is about 0.27. At full scale, these values correspond to 4.6 mm and 1.37 cm, respectively.

In order to analyse the downslope motion of the bulge, the velocity of the front of the bulge u_B, the toe height x_2^T and its time derivative $\mathrm{d}x_2^T/\mathrm{d}t$ are calculated and

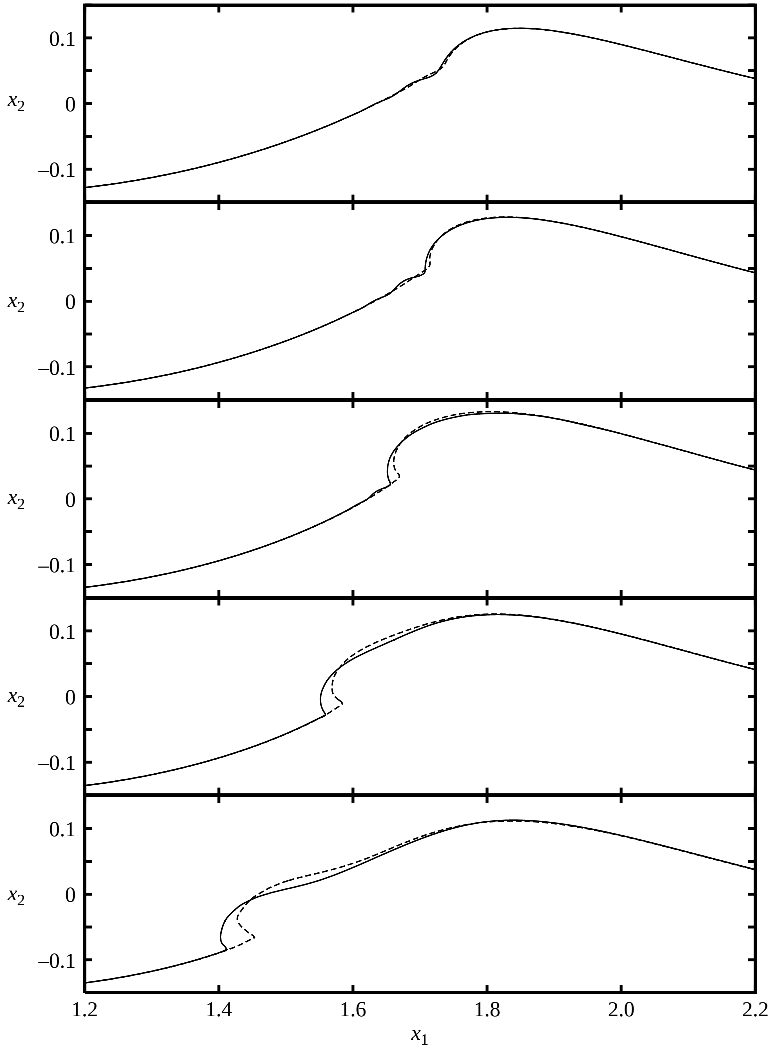

FIGURE 14. Effect of the thickness of the transition region on the wave breaking establishment ($We = 10.55$). From top to bottom $t = 11.5$, 12, 12.5, 13, 13.5. The use of a smaller thickness of the transition region (—, $\delta_T = \delta_P = 0.01$; - - -, $\delta_T = \delta_P = 0.02$) captures parasitic capillary waves in front of the toe which, however, are entrapped by the bulge during its downslope motion. The dynamics of the bulge motion is slightly faster in the former case.

their time histories are shown in figure 16 for the two different values of the thickness of the transition region. Although the bulge motion appears somewhat faster when using smaller values of δ_T and δ_P, the global behaviour looks essentially the same. The velocity of the front of the bulge u_B, evaluated as the horizontal velocity of the foremost point of the bulge profile and shown in figure 16(*a*), displays an acceleration phase followed by a region with a nearly constant velocity and, finally, a deceleration stage which lasts up to the foremost position of the toe (see figure 13). The existence of a central region with a nearly constant velocity is more evident in the simulation with the smaller thickness, plotted with a solid line.

The downslope motion of the bulge has been analysed and discussed also in Duncan *et al.* (1999) in the framework of gentle spilling breakers produced by the

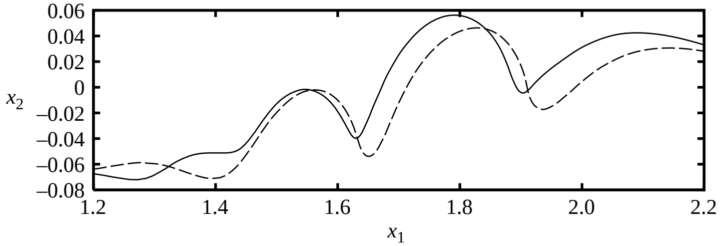

FIGURE 15. Comparison of the free-surface profiles in a later stage of the wave-breaking establishment for the cases shown in figure 14. In order to account for the faster dynamics of the solution with the smaller thickness, the profiles refer to different time instants being —, $t = 15.2$ for the case $\delta_T = \delta_P = 0.01$ and - - -, $t = 15.6$ for the case $\delta_T = \delta_P = 0.02$. In spite of the phase shift in their generation, the amplitude and wavelength of the free-surface fluctuations are essentially the same. As the reference value for lengths is $L_r = 5.075$ cm, the amplitude and wavelength of the fluctuations at full scale can be estimated about 4.6 mm and 1.37 cm, respectively.

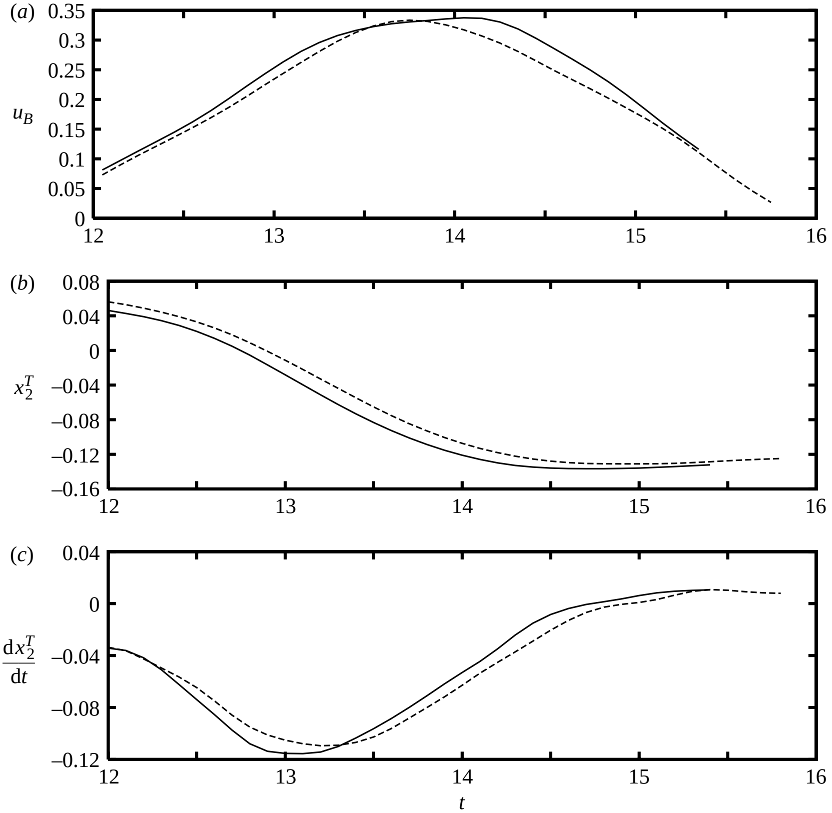

FIGURE 16. Comparison of the time histories of the horizontal velocity component u_B, of the toe height x_2^T and of its time derivative dx_2^T/dt, obtained by using two different values for the thickness of the transition region, —, $\delta_T = \delta_P = 0.01$ and - - -, $\delta_T = \delta_P = 0.02$. The velocity u_B is measured in the frame of reference attached to the hydrofoil.

wave-focusing technique. Therein, the downslope motion of the bulge is evaluated in terms of the time history of the toe height x_2^T and it is found that, just after the beginning of the toe motion, the toe height seems to follow a straight line with

$\mathrm{d}x_2^T/\mathrm{d}t \sim 0.135U$, where U is the carriage speed (i.e. the crest speed). With the aim of establishing a comparison with the results reported in Duncan *et al.* (1999), the toe height and its time derivative are extracted from the numerical results and plotted on figures 16(*b*) and 16(*c*), respectively. Also in terms of toe height, after an acceleration stage, a region with a nearly constant velocity value can be found with a maximum non-dimensional value $\mathrm{d}x_2^T/\mathrm{d}t \sim 0.11$. By comparing figure 16(*c*) with figure 16(*a*), it can be seen that the region with a nearly constant $\mathrm{d}x_2^T/\mathrm{d}t$ occurs before that in terms of u_B. This is probably because the bulge is sliding upon the forward face of the wave which is not straight.

A detailed experimental study of the flow field beneath the free-surface fluctuations developing behind spilling breakers has been provided by Duncan and his coworkers for gentle spilling breakers produced through a dispersive focusing method (Duncan *et al.* 1994, 1999; Qiao & Duncan 2001). These experiments clearly display the presence of a capillary wavetrain ahead of the toe, concurrent with the growth of the bulge. Then, the toe begins to slide down along the forward face of the wave and, during this downslope motion, a train of organized fluctuations develops between the toe and the crest (Duncan *et al.* 1999).

Numerical results presented above exhibit strong similarities with what is experimentally found. Free-surface fluctuations appear only after the toe has experienced its downslope motion and propagates downstream afterward. However, a better understanding of their nature can only be achieved by performing a more refined analysis of the space–time behaviour of the free-surface fluctuations.

3.5. *Spectral analysis of free-surface fluctuations behind microbreakers*

Small-scale surface fluctuations taking place behind breaking waves has received attention in quite distinct research frameworks, from naval hydrodynamics to geophysical applications, with many papers primarily concerned with the remote sensing, radar or infrared, of the ocean (see Banner & Fooks 1985; Siddiqui *et al.* 2001 for instance).

Among this body of literature, Walker *et al.* (1996) and Coakley & Duncan (1996) analyse surface fluctuations generated behind small-scale wave-breaking flows produced by submerged hydrofoils. With the aim of evaluating the main features of the downstream propagation, spectral analyses in space and time are performed on the basis of the instantaneous measurements of the free-surface elevation immediately ahead of and behind the breaking region. The occurrence of free-surface fluctuations behind breaking waves produced by a submerged hydrofoil has been also experimentally studied by Duncan & Dimas (1996), although the generation mechanisms and the shape of the spectra at fixed longitudinal positions behind the breaker, either in terms of surface height and velocity fluctuations, are primarily analysed therein.

The experimental analysis carried out in Walker *et al.* (1996), Coakley & Duncan (1996) and Duncan & Dimas (1996), being essentially focused on the understanding of the flow features in the quasi-steady regime, refer to a period of time much later than that of the first downslope motion of the toe. In table 2, their experimental conditions are summarized along with those used in the present numerical calculations. Several values of the submergence and of the angle of attack of the hydrofoil are used in the experiments leading to a rather broad range of wave-breaking intensities. The observed space–time behaviour of the free-surface profiles reveals two distinct components: (i) a low-frequency component, related to the surge motion of the toe; and (ii) a

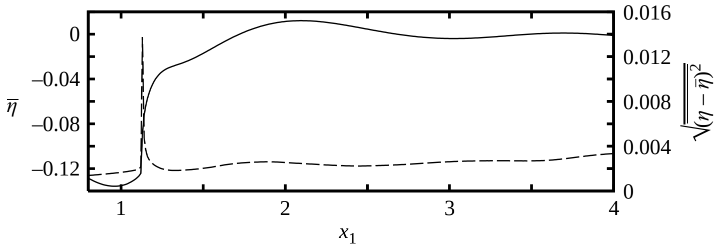

FIGURE 17. —, Average profile and - - -, r.m.s. fluctuation about the average. Owing to the sharp front of the bulge, large vertical fluctuations take place about $x_1 = 1.15$ as a result of the horizontal oscillation of the breaking region.

higher-frequency component, due to the downstream propagating free-surface fluctuations (Walker *et al.* 1996).

A similar spectral analysis is here performed on the numerical free-surface profiles. The free-surface elevation obtained for the numerical simulation at $Re = 2500$ is sampled with $\Delta t = 0.005$ in the interval $t = 37$ to $t = 56$ and, in space, with $\Delta x_1 = 0.01$ in the range $x_1 = 0.8$ to $x_1 = 4$. The horizontal extension of this window is chosen as large as one and half wavelengths provided by the linear theory, $\lambda_\infty = 2\pi U_r^2/g$, which corresponds to $\lambda_\infty = 10.25$ cm at full scale. The differences between the flow conditions used in the numerical calculations and those used in the experiments should be properly considered when comparing results (see table 2).

In figure 17, the averaged surface height $\overline{\eta}$ and the r.m.s. (root mean square) value of the fluctuations, $\sqrt{\overline{(\eta-\overline{\eta})^2}}$, are shown. Owing to the stronger surface tension and, presumably, to the much lower Reynolds number, the front of the bulge is much sharper with respect to the experimental results, thus giving rise to the large spike in the r.m.s. curve as a consequence of the horizontal oscillation of the toe (low-frequency component). This effect rapidly decays behind the toe. Downstream, the amplitude of fluctuations increases up to a maximum and then slightly oscillates with higher values at the crest and lower values at the troughs, in agreement with Duncan & Dimas (1996). It is shown later on that these fluctuations are mainly composed of the high-frequency contributions.

In order to establish a more quantitative comparison, the r.m.s. values of the free-surface fluctuations reported in Walker *et al.* (1996) and in Duncan & Dimas (1996) are non-dimensionalized by using the wavelength provided by linear theory for deep-water waves, that is $\lambda_\infty = 2\pi U_r^2/g$, as a reference value for lengths. Correspondingly, the r.m.s. value based on the numerical result, which is non-dimensionalized by the chord of the hydrofoil, is divided by the non-dimensional wavelength $\lambda_\infty = 2\pi Fr^2 = 2.02$.

In Walker *et al.* (1996), the maximum r.m.s. value of the fluctuations, found about the toe (properly non-dimensionalized by the corresponding wavelength) ranges from 0.0074 to 0.0102. Downstream, the r.m.s. value of the fluctuations decays, reaching a value which ranges from 0.0019 to 0.0033. For both quantities, higher values occur for a larger angle of attack, that is for stronger breaker intensities. In Duncan & Dimas (1996), the r.m.s. values of the fluctuations measured at the first and second trough of the following wave system are provided. The non-dimensional r.m.s. value of the fluctuations ranges from 0.0022 to 0.0040 and from 0.0020 to 0.0032 at the first and second trough, respectively, thus indicating a reduction of the fluctuations as they move downstream. From figure 17, the maximum r.m.s. value of the fluctuations

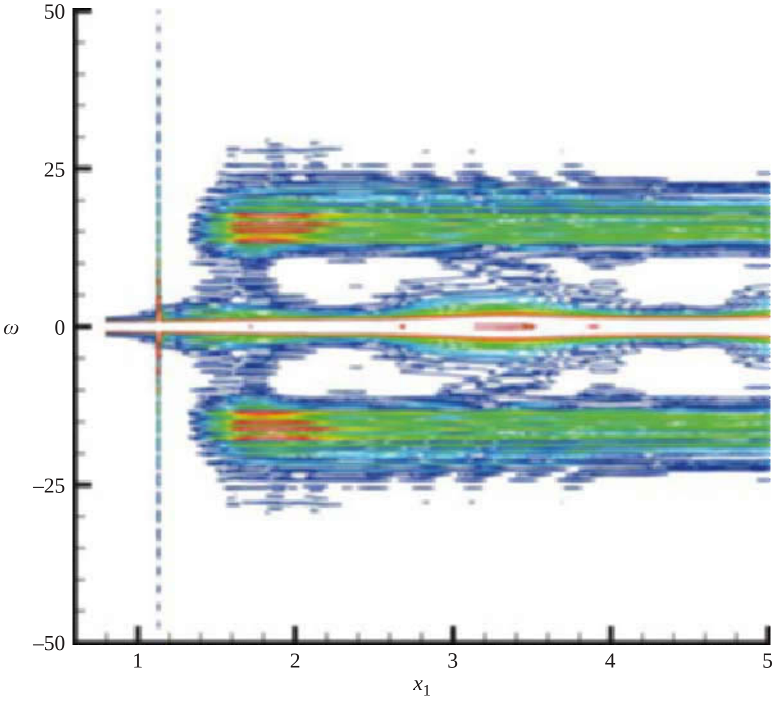

FIGURE 18. Frequency spectrum of the numerical results shown in figure 13. Fourier transforms are taken at different longitudinal positions in the frame of reference attached to the hydrofoil. As a result of the rather sharp front of the bulge, a broad spectrum is found about $x_1 = 1.15$.

taking place about the toe, divided by λ_∞, is 0.0069 while downstream the value decays up to 0.0015. The maximum value is in good agreement with that measured in Walker *et al.* (1996) while the r.m.s. value downstream appears somewhat smaller compared to those measured in Walker *et al.* (1996) and in Duncan & Dimas (1996). However, taking into account the large scatter of the r.m.s. values measured with different intensities of the breaker and the different flow conditions (namely profile type, angle-of-attack, profile depth) used in the experiments and in the computations, it is believed that differences are induced by a lower breaker intensity in the numerical results.

A better comprehension of the propagation mechanisms of free-surface fluctuations can be achieved by evaluating the Fourier transforms in time and space. Then, the wavenumber–frequency spectrum is evaluated as follows:

$$S(k_{x_1}, \omega) = \int\!\!\int \eta(x_1, t) \exp(\mathrm{i}(\omega t - k_{x_1} x_1)) \, \mathrm{d}\omega \, \mathrm{d}k_{x_1}.$$

In figure 18, the contours of the frequency components of the free-surface fluctuations are shown versus the streamwise location. This graph clearly displays the existence of the two distinct low- and high-frequency components. The low-frequency oscillation is due to the back and forth motion of the toe while the high frequency oscillation, centred about $|\omega| = 16$ rad per unit of time, is related to the downstream propagation of the fluctuations. The vertical contour levels about $x_1 = 1.15$ represent the broadband frequency components associated to the motion of the sharp front of the bulge (see figure 17).

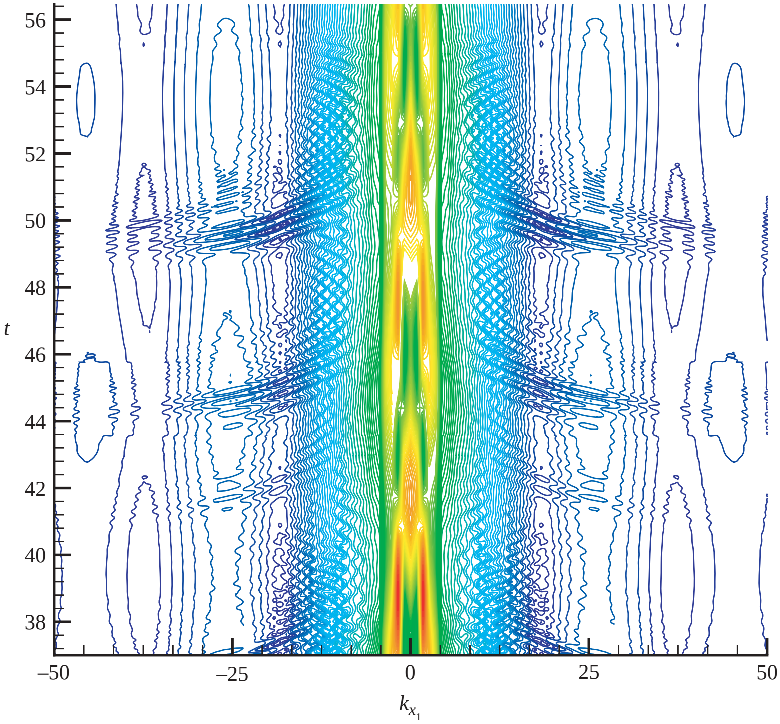

FIGURE 19. Wavenumber spectra evaluated at different times of the free-surface evolution of the numerical results shown in figure 13.

The high-frequency component is ascribed to the propagation of the free-surface fluctuations since this contribution only appears behind the crest of the bulge, as can be seen by comparing the graph in figure 18 with the average profile shown in figure 17. The frequency components associated to the formation and propagation of the fluctuations exhibit a rapid initial growth from $x_1 \sim 1.4$ to $x_1 \sim 1.8$. Further downstream, but for a weak reduction in the amplitude taking place up to $x_1 \sim 2.2$, they remain nearly constant. These results are in qualitative good agreement with those of Walker *et al.* (1996). The larger decay rate observed in the experiments can be attributed to the differences in the conditions, as reported in table 2, and to the two-dimensional assumption made in the present numerical computations.

With the aim of establishing a quantitative comparison with data measured by Walker *et al.* (1996) and by Duncan & Dimas (1996), the frequencies of the spectral peaks are non-dimensionalized by the frequency of the following wave $f_\infty = g/(2\pi U_r)$ provided by linear theory. In Walker *et al.* (1996), the non-dimensional value is about $f_p = 5.49$ (at least for an angle of attack of 3°) while in Duncan & Dimas (1996) it is found in the range 3.884 to 5.406, with the lower value measured for the stronger breaker intensities. From the numerical results reported in figure 18, the peak is located about $\omega = 16$ rad per unit of time, that is $f_p = 5.124$, a value which appears to be in good agreement with the experimental data. At full scale, the peak would occur at at frequency of about 20 s^{-1}.

With regard to the spatial Fourier transform, in figure 19, the wavenumber spectrum is displayed versus time. This picture clearly shows that, periodically, components at short wavelength appear about $|k_{x_1}| = 25$, which corresponds to a dimensional

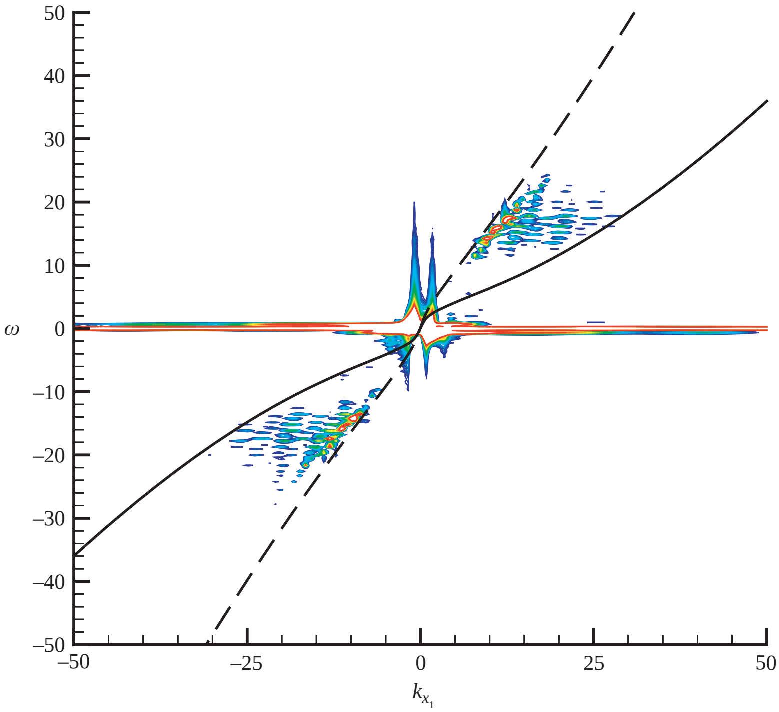

FIGURE 20. Wavenumber–frequency spectrum. The dispersion relation (3.3) is plotted in this graph for —, $U = 0$; - - -, $U = U_r$. By comparing this graph with the frequency spectrum it can be seen that the peaks about $k_{x_1} = 0$ correspond to the vertical line in figure 18 and then are related to the oscillation of the toe. The contribution due to the free-surface fluctuations is instead the well-identified region inside the two dispersion curves.

wavelength of about 1.27 cm. As time elapses, that is during the downstream propagation, the fluctuations' wavelength grows, in agreement with the discussion in Walker *et al.* (1996). The growth of the wavelength during the downstream propagation can be unambiguously seen by comparing the $(k_{x_1} - t)$ graph and the corresponding time history shown in figure 13. As an example, about $t = 43$, the time history clearly displays the generation of free-surface fluctuations. In the successive stage, until $t = 47$, the time history indicates that fluctuations propagate downstream growing in size and this is reflected in the shift of the wavenumber components from higher to lower values. The phenomenon is then repeated from $t = 49$.

Although the fluctuations' wavelength grows during their downstream motion, no substantial changes occur in terms of frequency components. This led Walker *et al.* (1996) to speculate that the behaviour is 'consistent with the idea of waves propagating on a spatially varying current'. In order to further support this idea, in Walker *et al.* (1996), the dispersion relation given by linear theory

$$\omega = \left(g k_{x_1} + \sigma k_{x_1}^3\right)^{1/2} + U k_{x_1}, \tag{3.3}$$

is plotted on the wavenumber–frequency spectra by assuming $U = 0$ and $U = U_r$. In figure 20, the same graph is drawn on the basis of the present numerical results. As already stated, the oscillating motion of the toe is associated with small frequencies while high-frequency components at short wavelength are instead induced by the sharpness of the bulge front. Downstream-propagating free-surface fluctuations manifest themselves at higher wavenumbers with ω ranging from 10 to 30.

As discussed in Walker *et al.* (1996), fluctuations are generated in the breaking region where the fluid is almost at rest in the hydrofoil frame of reference (Lin & Rockwell 1995) and the dispersion relation with $U = 0$ (solid line in figure 20) provides a higher bound for their wavenumber. As they propagate downstream, thus reducing the wavenumber components, the underlying current is accelerating and then the dispersion relation with $U = U_r$ is progressively approached (dashed line in figure 20).

On the basis of the above considerations, it follows that the main features of the wavenumber–frequency spectrum derived from numerical results are in a good agreement with that shown in Walker *et al.* (1996), starting from the experimental data. This gives confidence in the capability of the numerical approach to predict correctly the downstream propagation of free-surface fluctuations. However, as the numerical results discussed so far have been obtained through a two-dimensional model, an analysis of the inaccuracies related with this assumption should be made.

Free-surface profiles in the cross-stream direction have been measured in Coakley & Duncan (1996). From their analysis, it appears that there is a strong component aligned parallel to the wave crest, thus suggesting that the generation mechanism of the free-surface fluctuations is essentially two-dimensional. Nevertheless, an unavoidable limitation lying in the two-dimensional assumption is that vorticity structures cannot experience a three-dimensional breakdown, thus lasting for a longer time. This can be the reason why, in the numerical results, the r.m.s. value of the free-surface fluctuations, shown in figure 17, does not exhibit a significant decay in the downstream direction, in contrast to the $x_1^{-1/2}$ law experimentally found by Duncan & Dimas (1996).

With the aim of achieving a more complete comparison between the numerical and the experimental results reported in Duncan & Dimas (1996), the free-surface fluctuations taken at $x_1 = 1.75$ are used for deriving the power spectral density $P(\omega)$ as:

$$P(\omega) = \frac{|X(\omega)|^2}{T},$$

where $X(\omega)$ is the Fourier transform of the free-surface elevation and T is the time interval of the computed signal. In the inertial range, the power spectral density, plotted in figure 21, exhibits a decay which follows a -8 power law, which is much faster than the $-7/2$ decay law found in Duncan & Dimas (1996).

This aspect agrees with Duncan & Dimas (1996) when using a two-dimensional Euler solver to investigate the development of shear flow instabilities beneath the free surface. Even in their result, the computed spectrum decays faster than the $-7/2$ power law experimentally found. In spite of this difference, however, they conclude that the two-dimensional analysis correctly predicts the frequency of the spectral peak.

3.6. *Shear flow instabilities as a source of the free-surface fluctuations*

With the purpose of investigating the initial formation and the propagation of the fluctuations, a careful analysis of the flow field taking place beneath the free surface is carried out in the following. As shown in Duncan *et al.* (1999) when analysing their results, the generation of fluctuations does not appear until the toe motion begins its downslope motion, thus allowing authors to speculate that they are generated by the instabilities of the shear flow developing between the gravity-induced downslope flow near the surface and the underlying upslope flow.

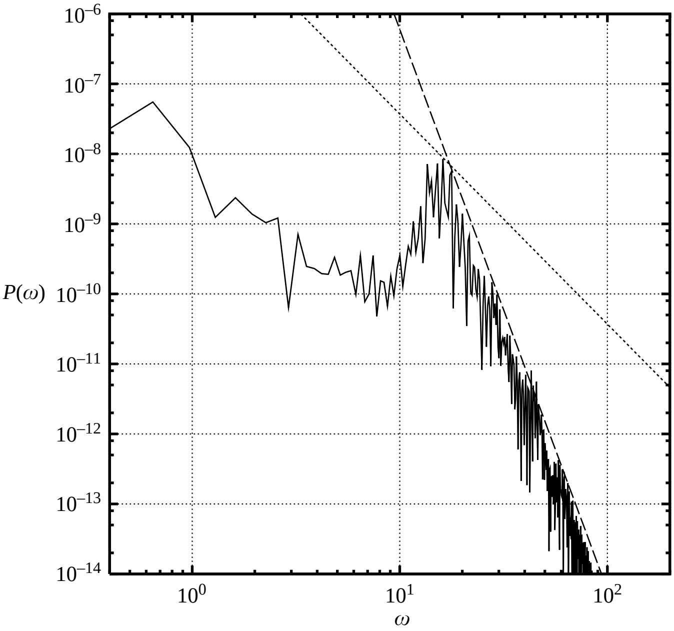

FIGURE 21. Spectral power of the free-surface fluctuations at $x_1 = 1.75$. The power laws $\ldots$, $\omega^{-7/2}$; - - -, ω^{-8} are also shown in the graph.

By following this consideration, in figure 22, for the simulation at $Re = 2500$, a sequence of vorticity fields is shown, from the initial downslope motion of the bulge until the appearance of the fluctuations. The instantaneous vorticity fields clearly display the initial growth of the instabilities of the shear flow developing between the fluid inside the bulge, which is moving upstream, and the incoming upslope flow. At a later stage, instabilities lead to the formation of separated coherent structures that strongly interact with the free surface, giving rise to the free-surface fluctuations which are traces of the vortex structure lying beneath. In particular, the interaction of the vortex structure with the free surface leads to the formation of a scar, which corresponds to the fluctuations' troughs, just downstream of the vortex structure itself.

In the early stage after their appearance, free-surface fluctuations grow in amplitude while the wavelength is essentially related to the distance between two adjacent coherent structures. Hence, the wavelength grows during the downstream motion of the vortex structures, owing to both the growing distance between adjacent structures and the diffusion process of the single structure. At a later stage, the intense interaction between vorticity and the highly curved free surface is responsible for the production of secondary vorticity shed into the water, highlighted by the last three configurations in figure 22.

For the sake of the clarity, an enlarged view is depicted in figure 23 where the vorticity multiplied by density contours are plotted, aimed at emphasizing the vorticity field in the water domain. From these graphs, it can be seen that the maximum intensity of the secondary vorticity can be larger than that of the corresponding primary structures. The generation of secondary vorticity displays strong similarities with the dipole–free-surface interaction discussed in § 3.1. The velocity field developing after secondary structures appear, acts to hold back the primary ones, thus leading to the formation of vortex pairs. Owing to the self-induced velocity field, vortex pairs

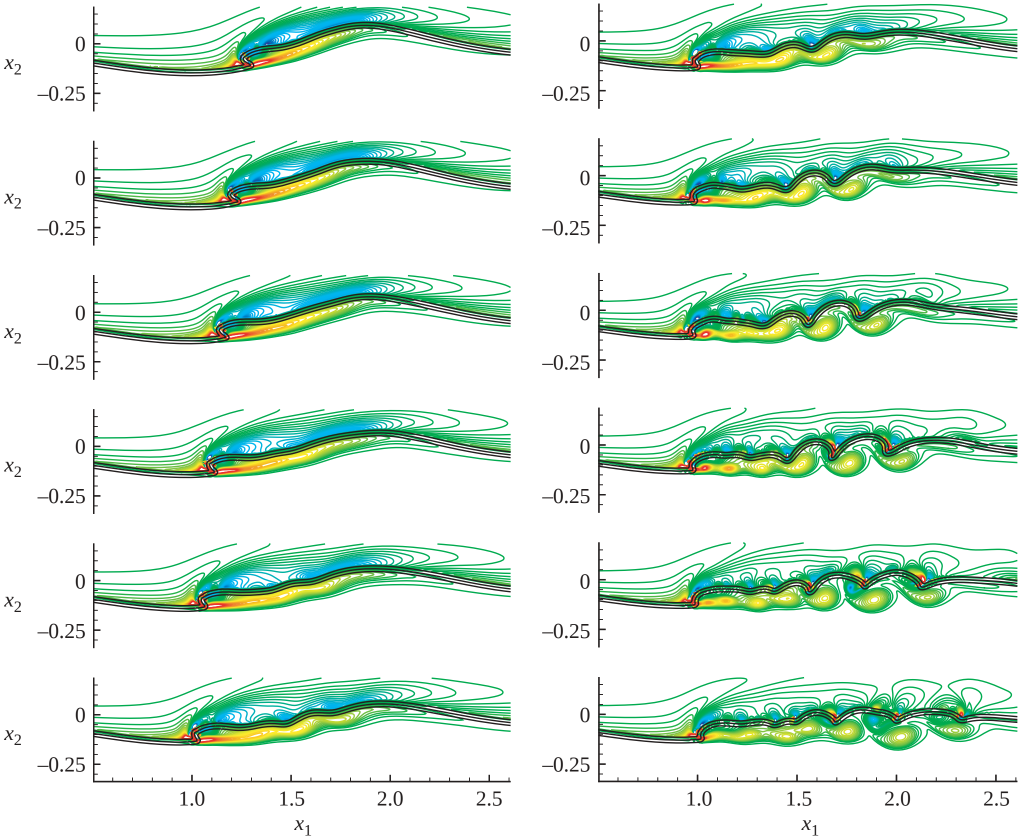

FIGURE 22. Sequence showing free-surface profiles and vorticity contours during the first downslope motion of the bulge, as seen in the hydrofoil frame of reference ($We = 10.55$, $Re = 2500$). Configurations refer to the interval $t = 14$ to $t = 16.2$ with a time step $\Delta t = 0.2$. The development of shear flow instabilities and the corresponding formation of free-surface fluctuations is clearly shown. Secondary vorticity also appears as a result of the interaction of primary coherent structures with the highly curved troughs.

are 'overtaken' by the associated troughs which, therefore, experience a reduction of their curvature.

The strong vorticity–free-surface interaction is responsible for the large asymmetry of the profiles of the free-surface fluctuations with respect to the horizontal axis, with smooth crests opposed to highly curved troughs. A relevant asymmetry of the troughs with respect to the vertical axis is also evident, as shown in figure 23. It is believed that the combined action of the gravity and of the surface tension prevents the entrapment of air and the cusp formation at the troughs (Longuet-Higgins 1989).

In order to characterize the shear layer originating at the toe, profiles of the velocity field at different stages of the back and forth motion of the bulge are plotted in figure 24. Vertical distributions of the horizontal velocity $u_1(x_2)$ are evaluated when: (i) the bulge is sliding down along the forward face; (ii) the bulge reaches its maximum forward position; (iii) the bulge is moving backward; (iv) the bulge reaches its maximum backward position. Velocity profiles are evaluated at the same horizontal distance Δx_1 from the toe and are plotted as a function of $x_2 - \eta(x_1)$ and are used for deriving an estimate of the shear-layer intensity as the ratio between the total velocity

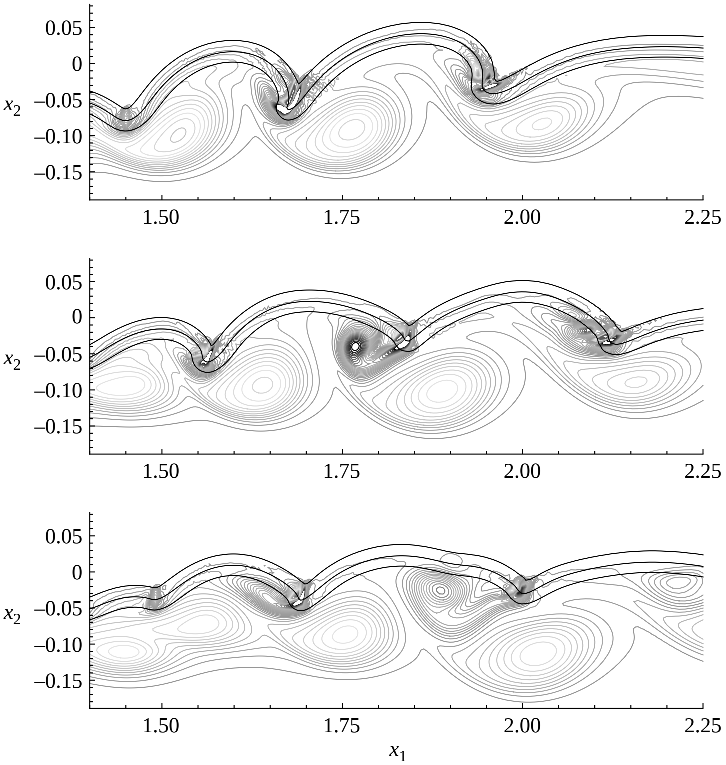

FIGURE 23. Enlarged views of the last three configurations of figure 22. Vorticity multiplied by density contours are drawn to emphasize the vorticity distribution in water.

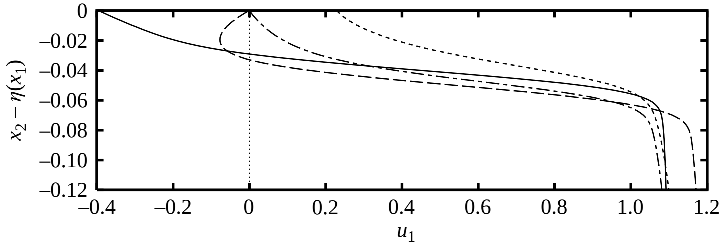

FIGURE 24. Plots of vertical cuts of the horizontal velocity component taken at a fixed distance from the toe ($\Delta x_1 = 0.1$). The four curves refer to different stages of the toe motion: —, forward motion; - - -, maximum forward position; . . . , backward motion; -·-, maximum backward position.

defect, $\Delta u_1 = u_{1\,max} - u_{1\,min}$, and the wake half-thickness, $b = x_2(u_{1\,mean}) - x_2(u_{1\,min})$. The above estimates are given in table 3 with regard to the four different stages of the bulge motion. As expected, stronger shear-layer intensities correspond to the downslope stage and to the rest at the foremost position.

4. Conclusions

In this paper, wave-breaking flows have been numerically studied with the help of an unsteady domain decomposition approach. In the free-surface sub-domain a

Phase	$\Delta u_1/b$
Forward motion	39.36
Maximum forward position	40.64
Backward motion	22.20
Maximum backward position	23.94

TABLE 3. Ratio between total velocity defect and the half-thickness of the wake relative to the velocity profiles shown in figure 24, relative to the four different stages of the toe motion.

two-fluid Navier–Stokes solver has been employed to handle the complex interface topologies taking place in the breaking and post-breaking regimes. The capability of the level-set technique and of the continuum model adopted for the surface tension contribution to predict accurately the interface motion in the presence of strong vorticity–free-surface interaction has been investigated and a careful validation has been performed on this. The accuracy and efficiency of the domain decomposition approach has been also proved by numerically simulating the regular wavy flow generated behind a submerged hydrofoil.

The proposed model has been applied to the investigation of scale effects on the flow features in the breaking-wave establishment. At the shortest scale, the mechanisms governing the wave-breaking development have been found to be substantially different from those observed at the larger scales. Air entrapment is entirely suppressed and the jet formation is replaced by a rounded bulge about the crest which slides down along the forward face of the wave, giving rise to a shear-layer development.

At the shortest scale, numerical simulations have been carried out at two different Reynolds numbers with the aim of investigating the role played by viscous effects. Downstream-propagating fluctuations, scarcely visible at the lowest Reynolds number, have been clearly identified at the higher one. Vorticity fields beneath the free surface taken at several times during the bulge motion unambiguously indicate shear-layer instabilities as being responsible for the free-surface fluctuations. Until now, this phenomenon has only been observed experimentally.

This work was supported by the Office of Naval Research, under grant *N*.000140010344, through Dr Pat Purtell and by the Ministero dei Trasporti e della Navigazione in the framework of the INSEAN Research Plan 2000-02. The authors wish to thank Professors J. H. Duncan, D. H. Peregrine and M. P. Tulin for the useful suggestions provided during the preparation of the manuscript.

REFERENCES

BANNER, M. L. & FOOKS, E. H. 1985 On the microwave reflectivity of small-scale breaking water waves. *Proc. R. Soc. Lond.* A **399**, 93–109.

BANNER, M. L. & PHILLIPS, O. M. 1974 On the incipient breaking of small scale waves. *J. Fluid Mech.* **65**, 647–656.

BATTJES, J. A. 1988 Surf-zone dynamics. *Annu. Rev. Fluid Mech.* **20**, 257–293.

BEST, J. P. 1993 The formation of toroidal bubbles upon the collapse of transient cavities. *J. Fluid Mech.* **251**, 79–107.

BONMARIN, P. 1989 Geometric properties of deep-water breaking waves. *J. Fluid Mech.* **209**, 405–433.

BRACKBILL, J. U., KOTHE, D. B. & ZEMACH, C. 1992 A continuum method for modeling surface tension. *J. Comput. Phys.* **100**, 335–354.

Brandt, A. 1992 Guide to multigrid development. *Multigrid Methods* (ed. W. Hackbush & U. Trottenberg), pp. 220–312. Springer.

Brocchini, M. & Peregrine, D. H. 2001 The dynamics of strong turbulence at free surfaces. Part 1. Description. *J. Fluid Mech.* **449**, 225–254.

Ceniceros, H. D. 2003 The effects of surfactants on the formation and evolution of capillary waves. *Phys. Fluids* **15**, 245–256.

Chen, G., Kharif, C., Zaleski, S. & Li, J. 1999 Two-dimensional Navier–Stokes simulation of breaking waves. *Phys. Fluids* **11**, 121–133.

Coakley, D. B. & Duncan, J. H. 1996 The flow fields in steady breaking waves. *Proc. 21st Symp. on Naval Hydrodyn.* pp. 534–549.

Duncan, J. H. 1981 An experimental investigation of breaking waves produced by a towed hydrofoil. *Proc. R. Soc. Lond.* A **377**, 331–348.

Duncan, J. H. 1983 The breaking and nonbreaking wave resistance of a two-dimensional hydrofoil. *J. Fluid Mech.* **126**, 507–620.

Duncan, J. H. 2001 Spilling breakers. *Annu. Rev. Fluid Mech.* **33**, 519–547.

Duncan, J. H. & Dimas, A. A. 1996 Surface ripples due to steady breaking waves. *J. Fluid Mech.* **329**, 309–339.

Duncan, J. H., Philomin, V., Behres, M. & Kimmel, J. 1994 The formation of spilling breaking water waves. *Phys. Fluids* **6**, 2558–2560.

Duncan, J. H., Qiao, H., Philomin, V. & Wenz, A. 1999 Gentle spilling breakers: crest profile evolution. *J. Fluid Mech.* **379**, 191–222.

Ebuchi, N., Kawamura, H. & Toba, Y. 1987 Fine structure of laboratory wind–wave surfaces studied using an optical method. *Boundary-Layer Met.* **39**, 133–151.

Hirt, C. W. & Nichols, B. D. 1981 Volume of fluid (VOF) method for dynamics of free boundaries. *J. Comput. Phys.* **39**, 201–221.

Iafrati, A. & Campana, E. F. 2003 A domain decomposition approach to compute wave breaking. *Intl J. Numer. Meth. Fluids* **41**, 419–445.

Iafrati, A., Di Mascio, A. & Campana, E. F. 2001 A level-set technique applied to unsteady free surface flows. *Intl J. Numer. Meth. Fluids* **35**, 281–297.

Jessup, A. T., Zappa, C. J. & Yeh, H. 1997 Defining and quantifying microscale wave breaking with infrared imagery. *J. Geophys. Res.* **102**, C10, 23 145–23 153.

Kim, J. & Moin, P. 1985 Application of a fractional-step method to incompressible Navier–Stokes equations. *J. Comput. Phys.* **59**, 308–323

Lafaurie, B., Nardone, C., Scardovelli, R., Zaleski, S. & Zanetti, G. 1994 Modelling merging and fragmentation in multiphase flows with SURFER. *J. Comput. Phys.* **113**, 134–147.

Lin, J. C. & Rockwell, D. 1995 Evolution of a quasi-steady breaking wave. *J. Fluid Mech.* **302**, 29–44.

Longuet-Higgins, M. S. 1989 Capillary–gravity waves of solitary type on deep water. *J. Fluid Mech.* **200**, 451–470.

Longuet-Higgins, M. S. 1992 Capillary rollers and bores. *J. Fluid Mech.* **240**, 659–679.

Longuet-Higgins, M. S. 1994 Shear instability in spilling breakers. *Proc. R. Soc. Lond.* A **446**, 399–409.

Melville, W. K. 1996 The role of surface-wave breaking in air–sea interaction. *Annu. Rev. Fluid Mech.* **28**, 279–321.

Mui, R. C. Y. & Dommermuth, D. G. 1995 The vortical structure of parasitic capillary waves. *J. Fluids Engng* **117**, 355–361.

Muscari, R. & Di Mascio, A. 2003 A model for the simulation of steady spilling breaking waves. *J. Ship Res.* **47**, 13–23.

Ohring, S. & Lugt, H. J. 1991 Interaction of a viscous vortex pair with a free surface. *J. Fluid Mech.* **227**, 47–70.

Okuda, K. 1982 Internal flow structure of short wind waves. Part I. On the internal vorticity structure. *J. Oceanogr. Soc. Japan* **38**, 28–42.

Peregrine, D. H. 1983 Breaking waves on beaches. *Annu. Rev. Fluid Mech.* **15**, 149–178.

Qiao, H. & Duncan, J. H. 2001 Gentle spilling breakers: crest flow field evolution. *J. Fluid Mech.* **439**, 57–85.

Quarteroni, A. & Valli, A. (Eds.) 1999 *Domain Decomposition Methods for Partial Differential Equations.* Oxford University Press.

Rai, M. M. & Moin, P. 1991 Direct simulations of turbulent flow using finite-difference schemes. *J. Comput. Phys.* **96**, 15–53.

Rapp, R. J. & Melville, W. K. 1990 Laboratory measurements of deep-water breaking waves. *Phil. Trans. R. Soc. Lond.* A **331**, 735–800.

Russo, G. & Smereka, P. 2000 A remark on computing distance functions. *J. Comput. Phys.* **163**, 51–67.

Scardovelli, R. & Zaleski, S. 1999 Direct numerical simulation of free surface and interfacial flow. *Annu. Rev. Fluid Mech.* **31**, 567–603.

Sethian, J. A. 1999 *Level Set Methods and Fast Marching Methods*. Cambridge University Press.

Siddiqui, M. H. K., Loewen, M. R., Richardson, C., Asher, W. E. & Jessup, A. T. 2001 Simultaneous particle image velocimetry and infrared imagery of microscale breaking waves. *Phys. Fluids* **13**, 1891–1903.

Sussman, M. & Dommermuth, D. G. 2000 The numerical simulation of ship waves using cartesian grid methods. *Proc. 23rd Symp. on Naval Hydrodyn.* pp. 762–779.

Sussman, M. & Fatemi, E. 1999 An efficient, interface-preserving level-set redistance algorithm and its application to interfacial incompressible fluid flow. *SIAM J. Sci. Comput.* **20**, 1165–1191.

Sussman, M. & Puckett, G. 2000 A coupled level-set and volume-of-fluid method for computing 3D and axisymmetric incompressible two-phase flows. *J. Comput. Phys.* **162**, 301–337.

Sussman, M., Smereka, P. & Osher, S. 1994 A level-set approach for computing solutions to incompressible two-phase flow. *J. Comput. Phys.* **114**, 146–159.

Tulin, M. P. 1996 Breaking of ocean waves and downshifting. *Waves and Nonlinear Processes in Hydrodynamics* (ed. J. Grue, B. Gjevik & J.E. Weber), pp. 170–190. Kluwer.

Unverdi, S. O. & Tryggvason, G. 1992 A front-tracking method for viscous, incompressible, multi-fluid flows. *J. Comput. Phys.* **100**, 25–37.

Walker, D. T., Lyzenga, D. R., Ericson E. A. & Lund, D. E. 1996 Radar backscatter and surface roughness measurements for stationary breaking waves. *Proc. R. Soc. Lond* A **452**, 1953–1984.

Zang, Y., Street, R. L. & Koseff, J. R. 1994 A non-staggered grid, fractional step method for time-dependent incompressible Navier–Stokes equations in curvilinear coordinates. *J. Comput. Phys.* **114**, 18–33.

Zhang, S., Duncan, J. H. & Chahine, G. L. 1993 The final stage of the collapse of a cavitation bubble near a rigid wall. *J. Fluid Mech.* **257**, 147–181.